Published in final edited form as:
Trends Analyt Chem. 2020 December ; 133: . doi:10.1016/j.trac.2020.116085.

Stretchable gas sensors for detecting biomarkers from humans and exposed environments

Ning Yi[a,1], **Mingzhou Shen**[b,1], **Daniel Erdely**[b], **Huanyu Cheng**[a,b,*]

[a]Department of Materials Science and Engineering, The Pennsylvania State University, University Park, PA, 16802, USA

[b]Department of Engineering Science and Mechanics, The Pennsylvania State University, University Park, PA, 16802, USA

Abstract

The recent advent of stretchable gas sensors demonstrates their capabilities to detect not only gaseous biomarkers from the human body but also toxic gas species from the exposed environment. To ensure accurate gas detection without device breakdown from the mechanical deformations, the stretchable gas sensors often rely on the direct integration of gas-sensitive nanomaterials on the stretchable substrate or fibrous network, as well as being configured into stretchable structures. The nanomaterials in the forms of nanoparticles, nanowires, or thin-films with nanometer thickness are explored for a variety of sensing materials. The commonly used stretchable structures in the stretchable gas sensors include wrinkled structures from a pre-strain strategy, island-bridge layouts or serpentine interconnects, strain isolation approaches, and their combinations. This review aims to summarize the recent advancement in novel nanomaterials, sensor design innovations, and new fabrication approaches of stretchable gas sensors.

Keywords

Stretchable gas sensor; Gas-sensitive nanomaterials; Direct integration; Stretchable structures; Gaseous biomarkers

1. Introduction

Recent developments of various gas sensing technologies have made it possible to detect gaseous biomarkers not only from the human body but also from the exposed environment. For example, a simple breath acetone sensor based on Si-doped WO_3 can accurately monitor body fat burning rates to provide real-time personalized and immediate exercise feedback [1]. With activated alumina powder as a filter to fast and highly selectively detect isoprene, the breath marker detected by this versatile sensor can be used to inform high blood

---

[*] Corresponding author. Department of Materials Science and Engineering, The Pennsylvania State University, University Park, PA, 16802, USA. huanyu.cheng@psu.edu (H. Cheng).
[1] These authors contributed equally to this work.

Declaration of competing interest
The authors declare that they have no known competing financial interests or personal relationships that could have appeared to influence the work reported in this paper.

cholesterol levels, influenza, endstage renal disease, muscle activity, lung cancer, and liver disease with advanced fibrosis [2]. Integration of multiple gas sensors in a small footprint array also has the capability to simultaneously detect various biomarkers with high precision, including acetone, ammonia, isoprene, carbon dioxide, and relative humidity released by respiration and skin below parts-per-million (ppm) levels [3,4]. The sensor array can be easily integrated into hand-held or drone-carried detectors to track the unique volatile chemical characteristics of trapped people for accelerated rescue work. In addition to the gaseous biomarkers from the metabolism of the human, hazardous gases in the exposed environment can also result in health issues when the exposure is beyond certain concentrations [5]. For instance, nitrogen dioxide (NO_2) frequently results in adverse respiratory health issues such as chronic bronchitis, emphysema, and irritation [6]. Studies also reveal a significant association between long-term NO_2 exposure and mortality due to heart failure and dysrhythmia [7,8]. As another example, formaldehyde, as one of the most important air pollutants in homes, is reported to be related to sick building syndrome, central nervous damage, and immune system disorders [9]. Furthermore, hydrogen sulfide (H_2S) is believed to cause a sore throat, cough, and eye irritation at a level of 10 ppm, and even be lethal for humans when the concentration is above the 700 ppm-level [10]. Other common hazardous gas compounds include acetone, methanol, toluene, sulfur dioxide (SO_2), ammonia (NH_3), and many others [11-13]. Corresponding gas sensors have also been reported for air quality monitoring (e.g., a highly selective hand-held gas sensor for methanol detection [1,14]).

Though the above gas sensors already exhibit excellent characteristics (e.g., high accuracy, fast response and recovery, good selectivity, low power consumption, small size, and low cost [15]), they are not easy to be miniaturized into a wearable form due to the need for a bulky electrochemical workstation [16]. The rising of stretchable electronics for monitoring of health-related parameters [17-22] has also led to the rapid development of stretchable gas sensors for continuous and real-time monitoring of the gaseous biomarkers from the human and dangerous gases in the exposed environment. With the advantages of real-time, continuous monitoring of relevant biomarkers, these stretchable gas sensors have the potential to provide very early medical diagnosis, significantly increasing the chances of successful treatment for widespread diseases such as lung cancer and melanoma, while decreasing the overall treatment costs [23]. Also, recurrent monitoring of important biomarkers with early interventions can help prevent the development of chronic illnesses such as asthma and circulatory system disorders [23]. In addition to the exhaled breath, stretchable gas sensors can also be applied to analyze skin hydration [24-26] and sweat composition [27,28].

From a material perspective, due to the dosimetric change of electrical resistance upon surface adsorption of gaseous analytes, a wide range of metal oxides with different chemical compositions and structures [29] have been reported as gas sensing materials with tunable sensitivity and selectivity [30]. The applications of metal oxide gas sensors include detecting explosives [31], the leakage of gaseous hazards [30-33] monitoring vehicle gas emission [34,35], among others. One of the most concerning aspects of the metal oxide-based gas sensors is their high working temperatures (e.g., 400° C, 250° C, and 200°C for SnO_2, CuO, and NiO, respectively) to ensure good sensitivity and fast gas desorption. However, high temperature is intrinsically not suitable for wearable sensing devices as the highest temperature that human skin can tolerate is around 43°C [36]. Thus, the wearable gas sensor is required to either have a thermal mitigation strategy to suppress the heat conduction to human skin or operate at reduced working temperature, at the same time, maintaining its gas sensing performance. Because of the response from the metal oxide to a wide range of gas molecules, most metal oxide gas sensors show compromised selectivity.

Carbon-based materials and transition metal dichalcogenides (TMD) in their 2D forms have been gaining momentum in the gas sensors due to their enhanced electron transfer [37], light-matter interaction [38], and surface-to-volume ratio [39]. The ultrathin thickness of 2D materials makes them ideal candidates for flexible gas sensors due to their large specific surface area and decent thickness close to the Debye length [40,41]. Thus far, the demonstrated gas or chemical vapor sensors have explored graphene [42], carbon nanotube (CNT), reduced graphene oxide (rGO) [43], as well as TMDs that include molybdenum disulfide (MoS_2) [44,45], molybdenum diselenide ($MoSe_2$) [46], tungsten sulfide (WS_2) [47]. Known as “synthetic metal,” conducting polymers such as polyaniline (PANI) [32,42,48], polypyrrole [49], and polythiophene [50] have been widely investigated on their gas sensing properties. Compared with other sensing materials, conducting polymers show advantages of high sensitivity and fast response rates at room temperature [51], which makes them attractive for wearable gas sensors. Other notable gas-sensitive materials also include layered group III-V semiconductor-based materials (e.g., GaS [52] and GaSe [53]) and semiconducting materials (e.g., black phosphorus [54] and silicon [55]), and composites that blend multiple types of sensing materials’ [13,56,57].

The development of stretchable gas sensors often relies on the direct integration of nanomaterials on a stretchable substrate or porous network, as well as being configured into a stretchable structure (Fig. 1). Other than silicone elastomers (e.g., polydimethylsiloxane (PDMS), Ecoflex) and textiles that are most frequently used for wearable electronics [58], the polyurethane (PU) elastomer with a comparable Young's modulus [59-61] and its electrospun forms of fibers or foams [62,63] also represent another promising substrate materials. Easy integration with these stretchable substrates has also led to extensive investigations of the aforementioned four types of sensing materials in the forms of nanoparticles, nanowires, or thin-films with nanometer thickness [64]. The synthesis of metal oxides with various nano geometries is extensively investigated [65], whereas TMD and carbon-based 2D materials can be fabricated through either chemical vapor deposition or mechanical exfoliation [66]. In addition to direct coating, chemical or electrochemical deposition can easily prepare thin films of conducting polymers [67]. A combination of these gas-sensitive nanomaterials with stretchable substrates or stretchable structures results in a new class of stretchable gas sensors, which can be placed onto the human body without device breakdown from mechanical deformations to inform the health conditions. This review aims to summarize the recent advancement in novel nanomaterials, sensor design innovations, and new fabrication techniques of stretchable gas sensors. The selected challenges (e.g., deconvolution of multiple gaseous species in a mixture) discussed in this review also represent a fraction of possibilities and opportunities for future development.

2. Direct deposition of gas-sensitive materials on stretchable substrates

2.1. Gas-sensitive materials on stretchable thin films

The most straightforward method to prepare stretchable gas sensors is to directly deposit gas-sensitive materials on soft elastomeric substrates such as silicone polymers. However, the stretchability of the resulting gas sensors is limited. Upon stretching, cracks often occur in the gas-sensitive thin films due to the rigid nature of most types of sensing materials (e.g., metal oxides, TMDs, and some conducting polymers). When the contact between cracked plates or regions is maintained during stretching, the device can still remain functional. One method is to explore the good adhesion between the cracked plates and soft elastomers, such as between zinc oxide (ZnO) plates and PDMS. The fabrication of this microtectonic ZnO-based stretchable gas sensor relies on the low adhesion of platinum (Pt) to the silicon substrate [68]. After a Pt layer is deposited on the silicon substrate, high-temperature ZnO films are sputtered and then peeled off with Pt using PDMS. Removing the Pt layer with reactive ion etching results in a ZnO-based stretchable gas sensor (Fig. 2a). The photography shows a transparent and twisted device without electrodes (Fig. 2b). When brittle oxide thin films are incorporated into the elastomeric substrate, the ZnO layer forms micrometer-sized plates with overlap that could slide over each other, as indicated by the microtectonic morphology of the ZnO surface (Fig. 2b). Due to the high adhesion to the elastomer, the microtectonic ZnO plates form a large functional surface and maintain electrical contact upon stretching. The fabricated sensor is able to sense both H_2 and NO_2 gases at room temperature *in situ* under sequential exposure to zero air, hydrogen, and nitrogen dioxide in a test chamber (Fig. 2c-i). The exposure of the sensor to H_2 results in a rapid drop in resistance and an exponential reverse recovery, whereas its exposure to NO_2 leads to a resistance increase with higher sensitivity, followed by a soft quadratic recovery (Fig. 2c-ii). Because the sensor exhibits opposite resistance changes when exposed to the two test gases (H_2 and NO_2), this characteristic could be used to distinguish these two gases under sequential exposure. However, it would still be challenging to deconvolute the two in a mixture as the combined responses may cancel either other. When the sensor is stretched to 5%, its sensitivity diminishes, though the response characteristics remain. High stability in the sensor response is observed in both relaxed and stretched states over multiple exposure cycles. The stretchable ZnO/PDMS gas sensor also exhibits larger sensitivity and faster response/recovery rates when compared to the rigid ZnO/silicon sensor. This superior sensing performance is attributed to the highly gas permeable nature of PDMS and the unique microtectonic morphology of the ZnO plates on PDMS, which both lead to an increased exposed surface area for gas sensing (Fig. 2c-iii). It should be noted that the demonstrated response process at room temperature is relatively short, when compared to its response curve at an elevated temperature of 100° C (Fig. 2c-iii). Thus, the room temperature response may be much slower. Nevertheless, this biocompatible gas sensor shows the potential to replace the current expensive hydrogen breath tests for *in vitro* detection of food intolerances.

To avoid device failure when stretched over a large tensile strain, gas-sensitive materials in the form of nanowires or nanoflakes have been investigated because of their robust conductive pathways preserved by the numerous junctions between nanowires/flakes [68].

For example, the bilayer conducting PANI consisting of planar PANI and aligned nanowires array is fabricated on a thin PDMS substrate through chemical bath deposition (Fig. 3a-i) [74]. Cracks are observed in the PANI thin film layer, whereas nanowires either cluster on top of the PANI film or bridge the gaps between cracked PANI islands (Fig. 3a-ii). Such a structure helps maintain the electrical conductivity of the PANI when the tensile strain is applied up to 100% (Fig. 3a-iii). The microstructural change of the PANI film is observed under a scanning electron microscope (SEM). As the tensile strain increases from 0% to 80%, the PANI thin film is fractured with increased crack and ridge density. However, the PANI islands are still interconnected through PANI nanowires in the gap (Fig. 3b). The sensitivity of the stretchable PANI gas sensor to CH_4 is examined under different tensile strain states (Fig. 3c). The conductivity of PANI significantly drops when exposed to CH_4 due to the deprotonation of PANI from its conducting emeraldine salt form to insulating emeraldine base form. It is interesting to note an increased sensitivity when the stretchable PANI sensor is stretched from 0% to 30% strain. A possible origin for such a phenomenon might be the exposure of fresh PANI upon stretching. However, an increase in the noise level is also observed as the sensor is stretched, which may cause the inaccurate reading of the gas concentration and compromise the limit of detection. Furthermore, the sensor could not be used to detect the gas concentration when the applied tensile strain is also changing during the gas concentration measurement as the sensor cannot differentiate the signal between the two. As a colorless and odorless volatile organic gas, CH_4 is frequently found in coal mines to cause potential safety issues. The burning or inhalation of CH_4 can also cause severe explosion or suffocation. Hence, the stretchable CH_4 gas sensors are of vital importance for safety and health monitoring.

Different from the above example that exploits nanowire array, nanofiber network (FN) is also highly desirable to enable mechanically flexible/stretchable properties in the gas sensors. Compared to electrospinning, the more cost-effective and efficient blow spinning technology prepares indium-gallium-zinc oxide (IGZO) FN on stretchable poly [styrene-b (ethylene-co-butylene)-b-styrene] (SEBS) substrates to result in a multifunctional sensor (Fig. 4) [75]. The highly stretchable conducting composite polystyrene sulfonate (PEDOT: PSS) used as the electric contacts in the sensor remains functional under various stretching deformation (Fig. 4a). The gas sensor is capable of detecting NO_2 gas and exhaled breath vapors. Its dynamic response to 20 ppm NO_2 demonstrates fast response and recovery rates of less than 50 s (Fig. 4b). The device is also highly selective to NO_2 in the presence of other nonoxidating gases (e.g., 20 ppm NH_3, 10^4 ppm CO_2, and 10^3 ppm H_2) (Fig. 4c). However, it should be noted that the normalized resistance change varies significantly and without a monotonic trend as the tensile strain is applied. When used as a temperature sensor, the IGZO FN exhibits a linear dependence on the temperature and higher sensitivity than the previously reported temperature sensors made of IGZO films, graphene (oxide)/polymer films, and P3HT/PDMS films (Fig. 4d). With a rapid current response to exhaled breath gas within 2 s, the sensor distinguishes different respiratory states from exhaled gas after physical activities (Fig. 4e). When breathing at a slow rate (~3–4 breaths min^{-1}), the current recovers to its initial value (~40 nA). In contrast, the current cannot fully recover and remains at a high level (300–6000 nA) of a normal respiratory rate (~15 breaths min^{-1}). For the jogging test, the IGZO FN device responds with an ~8 times increase in saturation current to reach ~5 × 10^4 nA, which is mainly due to the increased respiratory temperature and water vapor after exercise. The current change is also only 2–3 times of the minimum inhaling current of ~1.6 × 10^4 nA during rapid breathing. The wearable sensor can also detect human alcohol consumption. When tested at a slow breathing rate, the saturation current after drinking a 200 mL beer is 50% lower than that when not drinking, and the current change during inhaling and exhaling is 10–20 times lower than that without alcohol.

2.2. Gas-sensitive materials on stretchable textiles or porous templates

Besides stretchable thin films, stretchable textiles with entangled or interconnect fibers also provide some extent of stretchability due to the rotation of fibers upon stretching. The integration of sensing components on conductive fibers, yarns, and fabrics in clothes represents a new class of wearable electronics called electronic textiles (E-textiles). A simple and most commonly employed method for fabricating a textile-based stretchable gas sensor is to dip-coat gas-sensitive materials onto fibers by immersing the fibers in a well-dispersed solution of sensing material. Because of the highly porous fibrous materials with ample residing sites for dispersed sensing materials, the resulting stretchable gas sensor with high sensitivity from this facile fabrication process shows great potential for wearable gas detection when integrated onto clothes.

While the commonly used carbon-based materials (e.g., CNT, graphene, and rGO) have been explored in flexible and wearable E-textiles [76-78], the relatively weak adsorption strength between gas molecules and carbon-based materials often causes degraded gas sensing performance. One possible solution to this problem is to apply functionalization to the carbon-based materials for enhanced gas adsorption ability and tunable selectivity. For instance, the use of rGO/ZnO composite enhances sensitivity in the resulting stretchable gas sensing E-textile, where either commercial cotton threads (CT) or elastic threads (ET) is coated with rGO/ ZnO composite (Fig. 5a) [69]. Because the adhesion at the material interface is critical for the gas sensor to survive large deformation, (3-Aminopropyl)-triethoxysilane (APTES) has been explored as an adhesive layer between different materials. Briefly, the threads are firstly dip-coated with APTES (Fig. 5a-i) followed by GO dip coating (Fig. 5a-ii). Covalent bonding between the amino groups in APTES and carboxyl groups enhances the adhesion of GO onto the APTES coated fibers (inset, Fig. 5a-ii). Chemical reduction of GO into rGO (Fig. 5a-iii), followed by the dip-coating of APTES-ZnO, finishes the fabrication of the gas sensor (Fig. 5a-iv). SEM images indicate a uniform coating of rGO on both types of threads and subsequent successful attachment of ZnO onto rGO-coated cotton threads (Fig. 5b). The functionalized threads that can further be woven into the fabrics in a designed pattern (Fig. 5c-i) exhibit relatively small changes for a bending radius as small as 0.1 cm (Fig. 5c-ii) or a twisting angle as large as of 3600° (Fig. 5c-iii). The gas sensor can also be stretched to a tensile strain up to 100%, but the stretchinginduced shift of sensitivity is observed to be significant due to the large change in the resistance of the fibers from strain (Fig. 5c-iv). Knotting the gas sensing threads onto fabrics can further form an array of gas sensors (Fig. 5d). After obtaining a linear sensitivity from the rGO/ZnO sensor knotted by two sensing threads to NO_2 (Fig. 5d-i), a 4 × 4 sensor array is fabricated by knotting 4 perpendicular and 4 horizontal threads with each other (Fig. 5d-ii) stitched onto clothes (Fig. 5d-iii). The simultaneous NO_2 detection from multiple gas sensors promotes data reliability by minimizing the possible error from a single sensor, each with an experimentally demonstrated limit of detection of 100 parts-per-billion (ppb) (Fig. 5d-iv). Breakage or fracture of fibers can frequently happen due to the limited mechanical strength. However, knotting the broken fibers into each other can repair the gas sensor for further use, making the fiber-based gas sensor suitable for scalable gas sensing application.

Other than the commercial threads with a diameter in the micrometer range, textile-like fiber structures with a muchreduced diameter and increased specific surface area can also be prepared through an electrospinning process. By a simple ultrasonic-assisted dip-coating process (Fig. 6a), electrospun polyurethane (PU) nanofibers decorated with acidified carbon nanotubes (ACNTs) present good endurance to a maximum tensile strain of 100% (Fig. 6b) [60]. The sensitivity of the ACNTs-PU sensor to a relative humidity of 59% is observed to gradually increase with the increasing strain level (Fig. 6c), which is mainly caused by the increased hydrophilicity of the fiber surface upon stretching. Therefore, the relative humidity sensor with stretching-dependent sensitivity may only work at a given strain level to ensure accurate humidity measuring. After incorporating the fibrous sensor in a facemask, the sensing curves with different frequencies and magnitudes can be used to distinguish mouth from nose breathing, due to the lower breath frequency and more humid exhalation from the mouth breathing (Fig. 6d). The stretchable gas sensor is also capable of detecting different types of volatile organic compounds (VOCs), including methanol, heptane, acetone, toluene, and tetrahydrofuran (Fig. 6e). Though the sensor response to methanol is higher than those from the other VOCs and relative humidity, the interfering from the others cannot be ignored, especially when the target gas such as methanol is at a lower concentration. VOCs from human breath are important gaseous biomarkers of various types of diseases, including amoebic dysentery, intestinal bacterial infections, and cancer [79]. The non-invasive diagnosis of lung cancers and other diseases may be achieved by detecting the VOCs from human breath, when the limit of detection of the gas sensor is promoted to ppb level [80].

Similar to the textile structure, the 3D stretchable fibrous structure (e.g., sponges) is also suitable to serve as a template to integrate the sensing materials for stretchable gas sensors. As a representative example, silver nanowire (AgNW) and rGO can be dip-coated on the porous and interconnected PU sponges to yield a stretchable NO_2 gas sensor (Fig. 7a) [70]. As indicated in the SEM images of the PU sponge before and after the dip-coating process, the rGO/AgNW is successfully coated, where AgNW ensures continuous conductive pathways and moderate resistance (Fig. 7a). The sensitivity of the stretchable rGO/AgNW-PU gas sensor to NO_2 remains almost unchanged as the tensile strain is increased to 30%, but it increases significantly when the strain is further increased to 60% (Fig. 7b). This result indicates inaccurate detection when the strain is above 30%, as suggested by the authors. However, it could contribute to enhanced sensitivity and possibly lower limit of detection when the strain of 60% remains unchanged. Different from the oxidizing NO_2 gas, reducing gases such as acetone and ethanol donate electrons to rGO, causing a decrease of charge carriers (holes) and an increase of resistance (Fig. 7c, d). Compared to NO_2, the response curves of the rGO/AgNW-PU sensor to acetone and ethanol are associated with a higher level of noise, less accuracy, and different stretching-dependent sensitivity. Nevertheless, the stretchable rGO/AgNW-PU sensor exhibits good selectivity to NO_2 over VOCs (Fig. 7e).

3. Exploration of stretchable structures

3.1. Wrinkled structures created by the pre-strain strategy

Flexible thin-film materials can be rendered stretchable when they form a wrinkled structure by the pre-strain strategy. Briefly, after bonding the flat thin film on a uniaxially or biaxially prestrained soft elastomer, the release of the pre-strain transform the thin stiff film into a 3D buckled structure as the elastomer returns to its initial shape [81]. This simple strategy is directly applicable to 2D materials because of their extremely small thickness to enable easy bending and twisting during the formation of buckled structures. Because 2D materials cannot be easily synthesized on the soft polymeric substrate, they are firstly transferred from their growth substrate to the target soft substrate via the technique of transfer printing [82-84]. The low adhesion energy between 2D materials and silicone elastomer such as PDMS [85] has led to the use of a sacrificial layer to assist the transfer process.

Applying the uniaxial pre-strain strategy creates a crumpled quantum dot (CQD) sensing layer on the elastomeric substrate to result in a fully stretchable and humidity-resistant gas sensor (Fig. 8a) [71]. First, a rectangle-shaped VHB acrylic 4910 elastomer film is uniaxially stretched along one in-plane direction. Next, the graphene papers are dry transferred onto the substrate as electrodes due to their good intrinsic stretchability and low sheet resistance of ~200 Ω/sq. PbS CQDs are then deposited on the prestrained substrates as a functional sensing layer. The fabricated sensor can attach to a finger joint as the hand is in a “rock” and “paper” state. The sensor is also reversibly stretchable from wrinkled to flat states for repeated tensile cycling (Fig. 8b). Furthermore, the sensor has fast response and reversible recovery kinetics for 50 ppm NO_2 for uniaxial tensile strains of 0%, 44.4%, 54.5%, 61.5%, and 66.7% (Fig. 8c-i). Although the sensor remains functional to NO_2 of to 5 ppm, 10 ppm, 30 ppm, 50 ppm, 60 ppm, 80 ppm, and 100 ppm when stretched up to 90%, its sensitivity decreases compared to its counterpart without uniaxial tensile strain (Fig. 8c-ii). In addition to the negligible changes at the repeated uniaxial tensile strain (1000 times for 20% stretching) (Fig. 8c-iii), the sensor also highlights a humidity-resistant capability with a small variation in the response as the range of relative humidity increases from 0 to 86.7% for both 0 and 61.5% tensile strain (Fig. 8c-iv). The humidity-resistant capability of the gas sensor comes from the micro- and nano-scale hierarchical crumpled structures in the PbS CQD films, as evidenced by the increased static contact angles from 91.08° to 117.05° as the pre-strain increases from 0 to 61.5%. The combination of quantum dots with a crumpled layer provides a pathway for on-body wearable gas sensors due to their low working temperature and high sensitivity.

The application of the pre-strain strategy can also go from uniaxial to biaxial to prepare a biaxially stretchable chemiresistive WS_2-based humidity sensor on PDMS (Fig. 9a) [86]. The 2D WS_2 is first fabricated by sulfurization of W on the SiO_2/Si substrate and transferred to the intermediate PMMA substrate by etching the underlying SiO_2 layer. After attaching the PMMA/WS_2 laminate onto biaxially prestrained PDMS, etching away the PMMA by acetone accomplishes the assembly of WS_2/PDMS. Graphene interdigitated electrode (IDE) can be added on top of the WS_2 layer using the same PMMA-assisted transfer printing. The release of the pre-strain applied to PDMS results in a biaxially wrinkled structure for both the WS_2 layer and graphene IDE, yielding a stretchable humidity sensor that is functional under stretched, relaxed, and compressed states on the human wrist (Fig. 9b). In addition to an approximately identical response upon bending (Fig. 9c i-ii), the biaxially wrinkled WS_2 humidity sensor is also able to detect exhaled breath as a tensile strain increases from 0% to 40% (Fig. 9c iii-iv). The fast response rate and high sensitivity demonstrate the potential of the sensor for mask-free monitoring of human breath. Without a systematic characterization, the large fluctuation in the signal possibly comes from the resistance change in the sensor upon stretching or the variation in the exhaled breath.

3.2. Island-bridge layouts or serpentine connections

Besides the pre-strain strategy, the more advanced island-bridge layout is commonly explored for stretchable gas sensors, where the functional or sensing components fabricated on rigid islands are interconnected through serpentine conductive bridges. The serpentine bridges can unfold to follow the stretching deformation and accommodate the strain applied to the device system, while protecting the device components on rigid islands [72,86,87]. As an implementation of such a strategy, a multifunctional stretchable sensor system including a NO_2 gas sensor in the island-bridge layout is demonstrated, which is also self-powered by an array of micro-supercapacitors (MSCs) (Fig. 10a) [72]. The entire system consists of an array of nine MSCs, a radio frequency power receiver for charging the MSCs, and multiple sensors (Fig. 10b). In addition to a multi-walled carbon nanotube (MWNT)/SnO_2 NW sensor to detect both NO_2 and UV light, the sensing system also includes a fragmentized graphene foam sensor to detect biosignals (e.g., repeated human voice, pulse, and motion). These components on a single stretchable substrate are interconnected by embedded liquid metal. The NO_2 gas sensor shows a stable and almost unchanged response to NO_2 of 200 ppm even as the uniaxial tensile strain increases to 50%, demonstrating the mechanical stability of the integrated sensor system (Fig. 10c). Integrated with wirelessly rechargeable MSCs to power the sensors, this system demonstrates a great potential for self-powered NO_2 sensors and bioenvironmental monitors without a wired connection. However, it should be noted that the output voltage of the MSCs gradually decreases with time to result in a gradually decreased response to NO_2 gas over time.

A similar island-bridge layout has also been applied to a patterned-graphene NO_2 gas sensor powered by a polyaniline-wrapped MWNT (PWMWNT) micro-supercapacitor (MSC) integrated on a soft Ecoflex substrate (Fig. 11a) [87]. Because of the serpentine conductive Au bridges, the MSC and graphene gas sensors placed on a soft Ecoflex with embedded rigid SU-8 array can be stretched up to a maximum biaxial strain of 40% without causing device failure (Fig. 11b). Because of the significantly higher Young's Modulus of 4.1 GPa in SU-8 compared to that of silicone rubber of sub-MPa level [88], the rigid SU-8 islands isolate the large deformation from the underlying Ecoflex substrate and ensure a negligible deformation to protect the MSC and gas sensor. The evaluation of the graphene gas sensor to NO_2 under an increasing tensile strain from 0% to 50% also exhibits a gradually decreased sensitivity (Fig. 11c). It is noteworthy to point out that the decreased sensitivity may come from the continuous discharge of the MSC array during consecutive NO_2 exposures rather than the strain itself. Such a signal drift of gas sensors to the same concentration of target gas can also be attributed to the aging effect of the sensor [89] by environmental factors (e.g., humidity [90] and temperature [91]) and irreversible adsorption of gas molecules [92]. In the case of severe signal drifting that causes inaccurate measurement of target gas species, a drift compensation process for the data such as orthogonal signal correction is necessary to ensure valid readout of gas sensors by removing non-correlated variance [93]. The biaxially stretchable gas sensor can serve as a wireless body-attachable environmental monitor to detect NO_2 gas pollution.

Without directly using a stiff island, serpentine interconnects can also be applied to result in a stretchable gas sensor based on exfoliated 2D $MoSe_2$ with the sensing layer encapsulated by polyimide (PI) layers to locate at the neutral-mechanical plane (Fig. 12a) [94]. Positioned at the neutral mechanical plane, the sensing layer would experience a significantly lower level of strain upon bending [95]. After the fabrication of the $MoSe_2$-based gas sensor, the Au serpentine mesh connects the sensor to circuits on a flexible printed circuit board (flexible PCB) for data acquisition and processing, which further allows for conformal attachment on the forearm (Fig. 12bc). In addition to the exemplary n-type sensing curve of $MoSe_2$ (i.e., increased resistance and decreased current) to different concentrations of NO_2 (Fig. 12d), the gas sensor also highlights a nearly same sensitivity in the detection of NO_2 and NH_3 even when a tensile strain of 30% is applied (Fig. 12e). The result demonstrates superior mechanical stability and robustness of the stretchable gas sensor with the designs of serpentine interconnects and neutral mechanical plane. With the low-energy Bluetooth module embedded in the PCB, the sensing data can be transferred to an Android-based application and uploaded to the cloud. The capability of the sensor to detect NO_2 and NH_3 makes it suitable to protect asthma patients from the exacerbation of the respiratory system.

3.3. Strain isolation and its combination with serpentine structures

As evidenced by the aforementioned stretchable gas sensors, the effect of strain transduced from the substrate can play an important role in the sensitivity of gas sensors. Therefore, isolating the strain from the substrate provides an effective solution to the stretching-dependent sensitivity for a stretchable gas sensor. Placement of a strain isolation structure (e.g., a stiff [96] or soft [97] inclusion) between the sensing material and the underlying soft elastomeric substrate can help reduce the strain in the sensing layer as the substrate is stretched. As an example, the selective coating of rigid SU-8 around the gas-sensitive material (i.e., graphene/AgNW decorated with polypyrrole (PPy)) on a PDMS substrate forms a stretchable gas sensor with enhanced mechanical robustness (Fig. 13a) [98]. After transferring the chemical vapor deposition (CVD)-synthesized graphene onto the AgNWs on the PDMS, decorating PPy in the sensing region allows the gas sensor to sensitively and reversibly detect a nerve gas stimulant - dimethyl methylphosphonate (DMMP). The fabricated graphene-based field-effect transistor (FET) sensors exhibit different transfer characteristics in accordance to surface coating conditions (Fig. 13b). The PPy bonds to the graphene and target gas DMMP through π-π and hydrogen bondings, respectively. Without using the serpentine bridges, blending 2D materials with high aspect ratio conductive 1D materials such as metal NWs [99-101] also provides conductive, stretchable interconnects, which helps prevent failure of 2D materials caused by crack-induced open circuits. Pairing the graphene/ PPy gas sensor with a Bluetooth module enables wireless communication to monitor DMMP in real-time. Besides a fast response rate and a relatively linear sensitivity as the concentration of DMMP increases from 5 to 25 ppm (Fig. 13c), the hybrid graphene-PPy gas sensor also exhibits a good selectivity to DMMP against various organic gas molecules (Fig. 13d). The improved selectivity over that of pristine CVD-graphene [102] possibly comes from the higher chemical reactivity of PPy doped graphene. Because of the stretchable graphene/AgNW conductor and the strain isolation from the SU-8, only a negligibly small signal drifting occurs in the gas sensor response as it is stretched up to 20% (Fig. 13e). The integration of the gas sensor with a Bluetooth system and inductive antenna enables the immediate use of the gas sensor as smart Internet of things (IoTs) for environmental monitoring.

The strain isolation with a stiff inclusion can also be combined with serpentine interconnects for a stretchable gas sensor. The serpentine interconnects fabricated by a simple laser cutting of Au coated PI thin film can connect the gas-sensitive region to an external measurement setup on a soft elastomeric substrate with a rigid glass surface inclusion (Fig. 14) [103]. The gas-sensitive region explores interdigitated electrode (IDE) (with a gap of 80 μm between fingers) with drop-casted gas-sensitive nanomaterials (e.g., rGO/MoS_2 composites with controlled specific surface areas synthesized by a confined space solvothermal method). Besides bending and twisting (Fig. 14a), the gas sensor can also be stretched to 20% (Fig. 14b), with a very small variation in the sensitivity to NO_2 of different concentrations (Fig. 14c). A slight increase in the sensitivity and improvement in the calculated limit of detection is also observed at lower NO_2 concentrations upon stretching, possibly due to the strain effect on the nanomaterials. During a cyclic deformation test for a tensile strain of 20%, the resistance fluctuation is less than 1%, which is much smaller than the 6% response from NO_2 of 2 ppm to indicate a limited effect from the tensile strain of 20% (Fig. 14d). Though the response to 10 ppb NO_2 is small (i.e., ~0.1%), the rGO/MoS_2 gas sensor exhibits a high signal-to-noise ratio for ultrasensitive detection of NO_2 at ultralow concentrations (Fig. 14e). A good sensitivity against other common interfering gases is also observed in the rGO/MoS_2 gas sensor (Fig. 14f). The stretchable gas sensor with good selectivity, high sensitivity, and stretchability is suitable to detect NO_2 in the environment.

Compared to the conventional gas sensors with IDE and a separate heater, a novel laser-induced graphene (LIG) gas sensing platform can be prepared by a simple laser scribing process to significantly reduce the manufacturing complexity (Fig. 15a) [73]. The highly porous LIG with high specific surface areas in the sensing region can integrate various low-dimensional carbon-based or metal oxide nanomaterials to allow for highly sensitive detection of gases. The serpentine LIG interconnect can also be selectively coated with a thin film of metal (e.g., Ag) to significantly reduces its resistance. Because of the drastic resistance difference, the measurement voltage can easily induce self heating from a local Joule heating effect in the sensing area, which eliminates the need for a separate heater. While the sensitive nanomaterials (e.g., rGO/ MoS_2, rGO, MoS_2, or ZnO/CuO core/shell) are dispersed in the sensing region are the laser scribing, the nanomaterial precursor can also be applied on the PI substrate before the laser scribing. Nevertheless, the self-heating effect in the sensing region can easily increase the operating temperatures from 20 to 80°C (Fig. 15b). The dynamic response from the rGO/MoS_2-LIG gas sensor to NO_2 from 0.2 to 5.0 ppm indicates a monotonically increased response and a wide detection range for air quality monitoring and exhalation detection (Fig. 15c). Because of the existing PI beneath the LIG and the serpentine interconnection, the gas sensor can withstand a uniaxial tensile strain of 20% that corresponds to the maximum strain on the skin surface (Fig. 15d). Different from the selectivity for the rGO/MoS_2 (Fig. 15e), the ZnO/CuO core/shell on the LIG gas sensing platform exhibits a different selectivity (Fig. 15f), which could enable the electronic nose to deconvolute multiple gaseous components in a mixture. Other than the demonstrated strain isolation strategies, kirigami patterning [104] of the substrate and self-similar interconnect patterns [105] can also be applied to further enhance the strain isolation effect and reduce the resistance change in the LIG sensing region. When the strain-induced resistance change needs to be considered for the detection of target gases at ultralow concentrations, the concept from the electronic nose may also be applied to deconvolute the gas response from the strain. The facile and cost-effective fabrication method provides a novel gas sensing platform to enable stretchable gas sensors for various healthcare and environmental applications.

4. Applications of stretchable gas sensors

As a non-invasive medical monitoring and diagnostic method, the analysis of gaseous biomarkers starts to gain momentum for early diagnosis of various types of diseases. Among over 2600 gaseous biomarkers mostly from a single secretion pathway [23], there are already more than 10 biomarkers from the exhaled human breath (or skin perspiration) being used for disease diagnostics (Table 1). The commonly investigated gas species include acetone, ammonia, 2-butanone, ethanol, H_2S, NO, CO, H_2, NO_2, ethylene, menthone, styrene, trimethylamine, among others. A wide range of diseases has also been investigated, including diabetes [106], liver failure [107], helicobacter pylori [108], alcohol/cigarette consumption [109], asthma [110], lung injury [111], ovarian cancer [112], and chronic kidney disease [113]. The demonstrated success of stretchable gas sensors captures the gaseous biomarkers generated from metabolic processes in the exhaled breath or skin perspiration for non-invasive, portable, and personalized health monitoring and disease screening [114]. Electronic-nose based on metal oxide gas sensors [115], laser spectroscopy [116], gas chromatography-mass spectrometry (GC-MS) [117], and selected ion flow tube-mass spectrometry (SIFT-MS) [118] has already been applied for breath analysis. The GC-MS and SIFT-MS based methods are especially popular for identifying trace-VOCs due to their reliable identification and accurate quantification of a wide range of substances [118]. It is worth pointing out that practical analysis of breath or skin perspiration [23] requires the gas sensor to have both high selectivity and sensitivity. The former requirement comes from the fact of the significantly large number of gaseous biomarkers in the complex mixture, whereas the latter results from the exceptional low concentration of the target biomarkers (i.e., ~ ppb level). The demonstrated stretchable gas sensors have already shown the capability to detect NO_2 [68,69,73,75,103], methane [74], and NH_3 [94] down to 1.2 ppb [73], 10000 ppm [74], and 20 ppb [94], respectively. However, extensive efforts are still needed to detect more gaseous biomarkers with ultralow concentrations for the disease diagnostics. Furthermore, testing of the existing (stretchable) gas sensors still relies on a single type of calibration gas with known concentration, which is significantly different from the real complex gas mixture with multiple components.

Other than the biomarker detection, the stretchable gas sensor also highlights its potential in environmental air quality monitoring and industry safety, because their required detection limits are higher than the biomedical applications. For example, the demonstrated detection limit of 1.2 ppb to NO_2 is already well below the average NO_2 concentration of 50 ppb in the atmosphere [119]. Similarly, the demonstrated detection limit of 10000 ppm to methane is also below the lower and upper explosive limits of 5% and 15% (or 50000 ppm and 150000 ppm) in the air [120]. Therefore, the stretchable gas sensors can be readily applied for NO_2 detection and methane explosion alarm. Furthermore, some other gas species as environmental air pollution pose concerns to cause adverse health consequences. For instance, the excessive exposure to SO_2, O_3, and CO (average concentrations of 6 ppb, 32 ppb, and 770 ppb, respectively in the atmosphere [121]) can cause asthma, abnormal respiratory function, and chronic obstructive pulmonary disease [122].

5. Conclusion and future prospective

In this review, we present a glance over the state-of-the-art of the stretchable gas sensors for gaseous biomarker detection. These stretchable gas sensors are realized by integrating various gas-sensitive nanomaterials with soft elastomeric substrates and stretchable structures. Different stretchable strategies have shown their success in suppressing the effect of strain for accurate measurement. The representative strategies include direct deposition of gas-sensitive nanomaterials on stretchable thin film and porous templates (e.g., fabrics, sponges, or fibrous network), wrinkled structures from the pre-strain design, island-bridge layouts and serpentine interconnects, and various strain solation approaches. The performance of these stretchable gas sensors exhibits high sensitivity and selectivity, rapid response/recovery, and ultralow limit of detection. Because of these highperformance characteristics, they can accurately and continuously detect gaseous biomarkers from the human body, helping establish a direct pathway between health conditions and volatile biomarkers produced by the metabolism from the human. At the same time, these sensors can also detect potential harmful gases for environmental monitoring, industry safety, and military countermeasures.

Though a variety of nanomaterials has been applied for stretchable gas sensors, there is still a wide range of gas-sensitive nanomaterials commonly used in rigid gas sensors that are not explored in their stretchable counterparts. Besides the demonstrated 2D materials, many others (e.g., MXene [139], black phosphorus [140], WSe_2 [141], ReS_2 [142]) and their doped or decorated derivatives [143] have yet to be integrated into the stretchable gas sensors. Mixed metal oxides with low working temperatures and conducting polymers with good long-term stability may also provide distinct selectivity, high sensitivity, fast responses, and wide detection limits for a new class of stretchable gas sensors. The Schottky diode contacts, heterojunctions, and changed chemical composition within mixed oxides can lead to a remarkable change in the sensor sensitivity. For example, SnO_2–CuO porous nanotube gas sensor shows enhanced sensitivity and response rate to H_2S compared to SnO_2 gas sensors, possibly due to the synergistic effects and the significantly increased surface area [144]. Mixed-valence phases in molybdenum and tungsten oxide also exhibit enhanced sensitivity and selectivity to CO_2, with a tunable sensing performance by adjusting the ratio of molybdenum and tungsten [145]. In addition to the exploration of new sensing materials, room temperature sensing can also be achieved by the application of UV illumination. For example, the surface of metal oxides can be activated upon the UV excitation for room temperature sensing of various types of gas species [146] such as NO_2 [147], ethanol [148], and formaldehyde [149].

However, the material innovation itself may not be sufficient for the long-lasting challenge in the selectivity for chemiresistive or other types of gas sensors. The interference from other gas molecules in the sensor response to the target gas may limit the practical application of stretchable gas sensors because the ambient environment is always a mixture of multiple gas species. Efforts to address this grand challenge have led to the use of highly selective membranes [150] or catalytic filters [151], power laws-based analysis, and artificial neural networks (ANNs). By utilizing the extra molecular properties of the target analyte, the filter can significantly improve the selectivity of the gas sensor. For example, placement of a microporous zeolite membrane ahead of the nonspecific SnO_2-based sensors results in highly selective detection of formaldehyde [150]. This simple yet effective method allows for the accurate detection of formaldehyde with a concentration of 30 ppb at a relative humidity of 90% without interfering from 1 ppm ammonia, acetone, isoprene, or ethanol. Moreover, the coating of a nanoporous hydrophobic layer such as metal-organic framework (MOF) ZIF-8 over the gas-sensitive materials can effectively reduce the influence of humidity [152]. The facile design in the structure and property of MOF systems also allows them to selectively filter other types of gas molecules based on their size, shape, and chirality [153]. Therefore, MOF-based gas sensors have demonstrated excellent selectivity to NH_3, H_2, and H_2S [153-155]. Furthermore, hydrophilic and hydrophobic compounds [14] can be separated by an adsorptive packed bed column with polar nanostructured alumina, similar to the gas chromatography (GC) column. This design provides a highly selective detection of isoprene at a concentration of 5 ppb at 90% RH, although concentrations of methanol, ammonia, and acetone are much higher (e.g., 4–8 times) [2]. On the other hand, nonpolar adsorbents such as Tenax TA can separate molecules by molecular weight and chemical functional groups. They are widely used in air sampling, where heavy molecules are retained longer than lighter ones due to stronger adsorption by van-der-Waals forces [156]. While powerful, the application of catalytic filters and highly selective membranes is limited to a limited range of target gas species.

Power laws have been demonstrated to successfully explain the correlation between the response of gas sensors and the partial pressure (or concentration) of oxidizing/reducing gases [157]. Briefly, the response of a gas sensor can be expressed as a function of the partial pressure of target gas species $S_{gas} = 1 + \left[a * \left(\frac{P_{gas}}{P_{atm}}\right)^{b}\right]$, where S_{gas} is the response of the gas sensor, a and b are the coefficients to be determined by measuring the responses of the sensor at different partial pressures of target gas species (i.e., $Pgas$ and $Patm$). The response of a gas sensor to multiple gas species can then be expressed as the product of the responses to individual gas species due to their individual state functions [158], i.e., $S_{total} = S_{gas\,1} * S_{gas\,2} * S_{gas\,3}$ for three gaseous components in the mixture as an example. By building an array of three gas sensors, the response from the three sensors can be obtained as: $S_{j,\ Gas\_i} = 1 + [a_{ij} *(P_{Gas\_i}/P_{atm})^{b_{ij}}]$, where i = 1, 2, 3 represents the type of sensing material, and j =

1, 2, 3 represents the type of gas species. After determining the constants a_{ij} and b_{ij} (i, j = 1, 2, 3) from the sensor responses to various concentrations of individual gas species, the response of each gas sensor to the gaseous mixture can be expressed as $S_{i,\ total} = \Pi_{j=1}^{3}\left\{1+\left[a_{ji}*\left(\frac{P_{Gas\,j}}{P_{atm}}\right)^{b_{ji}}\right]\right\}$. For a mixture of the three predetermined gas species with unknown concentrations, the three unknown gas concentrations (i.e., $P_{\mathrm{Gas1}}/P_{\mathrm{atm}}$, $P_{\mathrm{Gas2}}/P_{\mathrm{atm}}$, and $P_{\mathrm{Gas3}}/P_{\mathrm{atm}}$) can be solved from the above equations.

Though power laws-based analysis can provide a quick and convenient method to determine gas concentrations from a mixture, a compromised accuracy [159] may hinder its application in scenarios where high accuracy is required. Errors of 7.12% and 22% are reported by the literature when gas sensor arrays are used to determine the concentration of NO_2 and CO within a mixture [159]. Such errors may come from the sensor instability, fitting inaccuracy, or possible reaction between the gases, which are difficult to prevent. As an alternative, ANNs provide a potential solution to detect the gas mixture. Compared to power law-based analysis, the ANNs-based model requires a much larger data set for the training of the model. However, the ANNs-based model can yield more accurate results (e.g., prediction error < 0.8 ppm with gas concentration ranging from 5 to 500 ppm) [160]. It is noteworthy that the number of neurons in the output (or input) layer of the ANNs model is determined as the number of gas species (or sensors). The number of neurons in the hidden layer can be determined through iterative testing of the ANNs for the most accurate layer configuration [161]. The convergence of novel stretchable gas sensors and big data analytics may offer a paradigm shift not only for the accurate deconvolution of multiple gaseous specious from the mixture, but also for large-scale and individualized correlation between the data and health. Nevertheless, the combination of novel gas-sensing nanomaterials, innovative device integration strategies, and big data analytics can lead to great strides in the burgeoning field of stretchable gas sensors for practical applications.

Acknowledgments

The review is written through the contributions of all authors. All authors have given approval to the final version of this review. This research is supported by National Science Foundation (Grant No. ECCS-1933072), the Doctoral New Investigator grant from the American Chemical Society Petroleum Research Fund (59021-DNI7), the National Heart, Lung, And Blood Institute of the National Institutes of Health under Award Number R61HL154215, and the start-up fund at The Pennsylvania State University. The partial support from the Center for Biodevices, the College of Engineering, the Institute for Computational and Data Sciences, the Center for Security Research and Education, Penn State Strategic Initiatives, the Materials Research Institute, and the Institutes of Energy and the Environment at Penn State is also acknowledged. The authors declare no conflict of interest.

References

[1]. Güntner A, Sievi NA, Theodore S, Gulich T, Kohler M, Pratsinis SE, Anal. Chem 89 (2017) 10578. [PubMed: 28891296]

[2]. van den Broek J, Güntner AT, Pratsinis SE, ACS Sens. 3 (2018) 677. [PubMed: 29443518]

[3]. Güntner AT, Pineau NJ, Mochalski P, Wiesenhofer H, Agapiou A, Mayhew CA, Pratsinis SE, Anal. Chem 90 (2018) 4940. [PubMed: 29601182]

[4]. Zhou X, Xue Z, Chen X, Huang C, Bai W, Lu Z, Wang T, J. Mater. Chem. B 8 (2020) 3231. [PubMed: 32031564]

[5]. Zheng X, Cheng H, Sci. China Technol. Sci 62 (2019) 209.

[6]. (a)Kong J, Franklin N, Zhou C, Chapline M, Peng S, Cho K, Dai H, Science 287 (2000) 622 10.1126/science.287.5453.622; [PubMed: 10649989] (b)Ko G, Kim H-Y, Ahn J, Park Y-M, Lee K-Y, Kim J, Graphene-based nitrogen dioxide gas sensors, Curr. Appl. Phys 10 (4) (2010) 1002–1004;(c)Weinmayr G, Romeo E, De Sario M, Weiland SK, Forastiere F, Short-term effects of PM_{10} and NO_2 on respiratory health among children with asthma or asthma-like symptoms: a systematic review and meta-analysis, Environ. Health Perspect 118 (4) (2009) 449–457. [PubMed: 20064785]

[7]. Brook RD, Rajagopalan S, Pope CA III, Brook JR, Bhatnagar A, Diez-Roux AV, Holguin F, Hong Y, Luepker RV, Mittleman MA, Circulation 121 (2010) 2331. [PubMed: 20458016]

[8]. Ljungman PL, Berglind N, Holmgren C, Gadler F, Edvardsson N, Pershagen G, Rosenqvist M, Sjögren B, Bellander T, Eur. Heart J 29 (2008) 2894. [PubMed: 19004842]

[9]. Li Y, Chen N, Deng D, Xing X, Xiao X, Wang Y, Sensor. Actuator. B Chem 238 (2017) 264.

[10]. Hu X, Zhu Z, Li Z, Xie L, Wu Y, Zheng L, Sensor. Actuator. B Chem 264 (2018) 139.

[11]. Mirzaei A, Leonardi S, Neri G, Ceram. Int 42 (2016) 15119.

[12]. Tyagi P, Sharma A, Tomar M, Gupta V, Sensor. Actuator. B Chem 224 (2016) 282.

[13]. Su P-G, Yang L-Y, Sensor. Actuator. B Chem 223 (2016) 202.

[14]. Van den Broek J, Abegg S, Pratsinis SE, Güntner A, Nat. Commun 10 (2019) 1. [PubMed: 30602773]

[15]. Stetter JR, Li J, Chem. Rev 108 (2008) 352. [PubMed: 18201108]

[16]. Baron R, Saffell J, ACS Sens. 2 (2017) 1553. [PubMed: 29025261]

[17]. Kumari P, Mathew L, Syal P, Biosens. Bioelectron 90 (2017) 298. [PubMed: 27931004]

[18]. Yi N, Cui H, Zhang LG, Cheng H, Acta Biomater. 95 (2019) 91. [PubMed: 31004844]

[19]. Sun R, Carreira SC, Chen Y, Xiang C, Xu L, Zhang B, Chen M, Farrow I, Scarpa F, Rossiter J, Adv. Mater. Technol 4 (2019) 1900100.

[20]. Zhou H, Zhang Y, Qiu Y, Wu H, Qin W, Liao Y, Yu Q, Cheng H, Biosens. Bioelectron (2020) 112569. [PubMed: 32905930]

[21]. Zhang L, Ji H, Huang H, Yi N, Shi X, Xie S, Li Y, Ye Z, Feng P, Lin T, ACS Appl. Mater. Interfaces 12 (40) (2020) 45504–45515. [PubMed: 32911929]

[22]. Zhang Y, Chen Y, Huang J, Liu Y, Peng J, Chen S, Song K, Ouyang X, Cheng G, Wang X, Lab Chip 20 (2020) 2635. [PubMed: 32555915]

[23]. Tricoli A, Nasiri N, De S, Adv. Funct. Mater 27 (2017) 1605271.

[24]. Yao S, Swetha P, Zhu Y, Adv. Healthc. Mat 7 (2018) 1700889.

[25]. Yamada Y, Hiyama S, Toyooka T, Takeuchi S, Itabashi K, Okubo T, Tabata H, Anal. Chem 87 (2015) 7588. [PubMed: 26176323]

[26]. D'amico A, Bono R, Pennazza G, Santonico M, Mantini G, Bernabei M, Zarlenga M, Roscioni C, Martinelli E, Paolesse R, Skin Res. Technol 14 (2008) 226. [PubMed: 18412567]

[27]. Oh SY, Hong SY, Jeong YR, Yun J, Park H, Jin SW, Lee G, Oh JH, Lee H, Lee S-S, ACS Appl. Mater. Interfaces 10 (2018) 13729. [PubMed: 29624049]

[28]. Wu J, Wu Z, Han S, Yang B-R, Gui X, Tao K, Liu C, Miao J, Norford LK, ACS Appl. Mater. Interfaces 11 (2018) 2364. [PubMed: 30596426]

[29]. Dey A, Mater. Sci. Eng., B 229 (2018) 206.

[30]. Korotcenkov G, Cho B, Sensor. Actuator. B Chem 244 (2017) 182.

[31]. Rashid T-R, Phan D-T, Chung G-S, Sensor. Actuator. B Chem 185 (2013) 777.

[32]. Ye Z, Jiang Y, Tai H, Guo N, Xie G, Yuan Z, J. Mater. Sci. Mater. Electron 26 (2015) 833.

[33]. Singh G, Choudhary A, Haranath D, Joshi AG, Singh N, Singh S, Pasricha R, Carbon 50 (2012) 385.

[34]. Kim J-W, Porte Y, Ko KY, Kim H, Myoung J-M, ACS Appl. Mater. Interfaces 9 (2017) 32876. [PubMed: 28882036]

[35]. Liu J, Li S, Zhang B, Xiao Y, Gao Y, Yang Q, Wang Y, Lu G, Sensor. Actuator. B Chem 249 (2017) 715.

[36]. Wienert V, Sick H, Zur Mühlen J, Anasthesie, Intensivtherapie, Notfall Med. 18 (1983) 88.

[37]. Choi W, Choudhary N, Han GH, Park J, Akinwande D, Lee YH, Mater. Today 20 (2017) 116.

[38]. Liu X, Galfsky T, Sun Z, Xia F, Lin E-C, Lee Y-H, Kéna-Cohen S, Menon VM, Strong light—matter coupling in two-dimensional atomic crystals, Nat. Photon 9 (1) (2015) 30.

[39]. Lee K, Gatensby R, McEvoy N, Hallam T, Duesberg GS, Adv. Mater 25 (2013) 6699. [PubMed: 24027114]

[40]. Zhao Y, Song J-G, Ryu GH, Ko KY, Woo WJ, Kim Y, Kim D, Lim JH, Lee S, Lee Z, Nanoscale 10 (2018) 9338. [PubMed: 29737989]

[41]. Zhang L, Khan K, Zou J, Zhang H, Li Y, Adv. Mater. Interf 6 (2019) 1901329.

[42]. Yoon HJ, Yang JH, Zhou Z, Yang SS, Cheng MM-C, Sensor. Actuator. B Chem 157 (2011) 310.

[43]. Lu G, Park S, Yu K, Ruoff RS, Ocola LE, Rosenmann D, Chen J, ACS Nano 5 (2011) 1154. [PubMed: 21204575]

[44]. Shokri A, Salami N, Sensor. Actuator. B Chem 236 (2016) 378.

[45]. Yan H, Zhong M, Lv Z, Wan P, Small 13 (2017) 1701697.

[46]. Choi SY, Kim Y, Chung H-S, Kim AR, Kwon J-D, Park J, Kim YL, Kwon SH, Hahm MG, Cho B, ACS Appl. Mater. Interfaces 9 (2017) 3817. [PubMed: 28058836]

[47]. Li X, Li X, Li Z, Wang J, Zhang J, Sensor. Actuator. B Chem 240 (2017) 273.

[48]. Zhang T, Qi H, Liao Z, Horev YD, Panes-Ruiz LA, Petkov PS, Zhang Z, Shivhare R, Zhang P, Liu K, Nat. Commun 10 (2019) 1. [PubMed: 30602773]

[49]. Xue M, Li F, Chen D, Yang Z, Wang X, Ji J, Adv. Mater 28 (2016) 8265. [PubMed: 27387035]

[50]. Zhang Y, Bunes BR, Wu N, Ansari A, Rajabali S, Zang L, Sensor. Actuator. B Chem 255 (2018) 1814.

[51]. Sonkusare AG, Tyagi S, Mishra S, Kaur M, Kumar R, Int. J. Appl. Environ. Sci 13 (2018) 59.

[52]. Yang S, Li Y, Wang X, Huo N, Xia J-B, Li S-S, Li J, Nanoscale 6 (2014) 2582. [PubMed: 24463644]

[53]. Yang S, Yue Q, Cai H, Wu K, Jiang C, Tongay S, J. Mater. Chem. C 4 (2016) 248.

[54]. Mayorga-Martinez CC, Sofer Z, Pumera M, Angew. Chem. Int. Ed 54 (2015) 14317.

[55]. Fahad HM, Shiraki H, Amani M, Zhang C, Hebbar VS, Gao W, Ota H, Hettick M, Kiriya D, Chen Y-Z, Sci. Adv 3 (2017), e1602557. [PubMed: 28378017]

[56]. Pang Z, Yang Z, Chen Y, Zhang J, Wang Q, Huang F, Wei Q, Colloid. Surface. A Physicochem. Eng. Aspect 494 (2016) 248.

[57]. Hua C, Shang Y, Wang Y, Xu J, Zhang Y, Li X, Cao A, Appl. Surf. Sci 405 (2017)405.

[58]. Liu Y, Pharr M, Salvatore GA, ACS Nano 11 (2017) 9614. [PubMed: 28901746]

[59]. Johnston I, McCluskey D, Tan C, Tracey M, J. Micromech. Microeng 24 (2014), 035017.

[60]. Huang X, Li B, Wang L, Lai X, Xue H, Gao J, ACS Appl. Mater. Interfaces 11 (2019) 24533. [PubMed: 31246404]

[61]. Rimai D, DeMejo L, Vreeland W, Bowen R, Gaboury S, Urban M, J. Appl. Phys 71 (1992) 2253.

[62]. Pedicini A, Farris RJ, Polymer 44 (2003) 6857.

[63]. Ugarte L, Saralegi A, Fernández R, Martín L, Corcuera M, Eceiza A, Ind. Crop. Prod 62 (2014) 545.

[64]. Qiao X, Chen X, Huang C, Li A, Li X, Lu Z, Wang T, Angew. Chem 131 (2019) 16675.

[65]. Carpenter MA, Mathur S, Kolmakov A, Metal Oxide Nanomaterials for Chemical Sensors, Springer Science & Business Media, 2012.

[66]. Joshi N, Hayasaka T, Liu Y, Liu H, Oliveira ON, Lin L, Microchim. Acta 185 (2018) 213.

[67]. Lv A, Pan Y, Chi L, Sensors 17 (2017) 213.

[68]. Gutruf P,Zeller E,Walia S,Nili H,Sriram S,Bhaskaran M,Small 11 (2015)4532. [PubMed: 26044575]

[69]. Li W, Chen R, Qi W, Cai L, Sun Y, Sun M, Li C, Yang X, Xiang L, Xie D, ACS Sens. 4 (2019) 2809. [PubMed: 31566369]

[70]. Luan Y, Zhang S, Nguyen TH, Yang W, Noh J-S, Sensor. Actuator. B Chem 265 (2018) 609.

[71]. Song Z, Huang Z, Liu J, Hu Z, Zhang J, Zhang G, Yi F, Jiang S, Lian J, Yan J, ACS Sens. 3 (2018) 1048. [PubMed: 29737152]

[72]. Kim D, Kim D, Lee H, Jeong YR, Lee SJ, Yang G, Kim H, Lee G, Jeon S, Zi G, Adv. Mater 28 (2016) 748. [PubMed: 26641239]

[73]. Yang L, Yi N, Zhu J, Cheng Z, Yin X, Zhang X, Zhu H, Cheng H, J. Mater. Chem. A 8 (2020) 6487.

[74]. Cai G, Wang J, Lin M-F, Chen J, Cui M, Qian K, Li S, Cui P, Lee PS, NPG Asia Mater. 9 (2017) e437.

[75]. Wang BH, Thukral A, Xie ZQ, Liu LM, Zhang XN, Huang W, Yu XG, Yu CJ, Marks TJ, Facchetti A, Nat. Commun 11 (2020) 1. [PubMed: 31911652]

[76]. Tang Z, Yao D, Du D, Ouyang J, J. Mater. Chem. C 8 (2020) 2741.

[77]. Wang B, Facchetti A, Adv. Mater 31 (2019) 1901408.

[78]. Wang X, Li Y, Pionteck J, Zhou Z, Weng W, Luo X, Qin Z, Voit B, Zhu M, Sensor. Actuator. B Chem 256 (2018) 896.

[79]. Wilson AD, Sensors 18 (2018) 2613.

[80]. Qiao X, Su B, Liu C, Song Q, Luo D, Mo G, Wang T, Adv. Mater 30 (2018) 1702275.

[81]. Fu H, Nan K, Bai W, Huang W, Bai K, Lu L, Zhou C, Liu Y, Liu F, J. Wang, Nat. Mater 17 (2018) 268.

[82]. Carlson A, Bowen AM, Huang Y, Nuzzo RG, Rogers JA, Adv. Mater 24 (2012) 5284. [PubMed: 22936418]

[83]. Zhou H, Qin W, Yu Q, Cheng H, Yu X, Wu H, Nanomaterials 9 (2019) 283.

[84]. Gao Y, Cheng H, J. Electron. Packag 139 (2017).

[85]. Choi T, Kim SJ, Park S, Hwang TY, Jeon Y, Hong BH, Nanoscale 7 (2015) 7138. [PubMed: 25811393]

[86]. Guo H, Lan C, Zhou Z, Sun P, Wei D, Li C, Nanoscale 9 (2017) 6246. [PubMed: 28466937]

[87]. Yun J, Lim Y, Jang GN, Kim D, Lee S-J, Park H, Hong SY, Lee G, Zi G, Ha JS, Nanomater. Energy 19 (2016) 401.

[88]. Xu T, Yoo JH, Babu S, Roy S, Lee J-B, Lu H, J. Micromech. Microeng 26 (2016) 105001.

[89]. Bhatia S, Verma N, Bedi R, Mater. Res. Bull 88 (2017) 14.

[90]. Suematsu K, Ma N, Watanabe K, Yuasa M, Kida T, Shimanoe K, Sensors 18 (2018) 254.

[91]. Yang S, Jiang C, Wei S.-h., Appl. Phys. Rev 4 (2017), 021304.

[92]. Wen C, Ye Q, Zhang S-L, Wu D, Sensor. Actuator. B Chem 223 (2016) 791.

[93]. Padilla M, Perera A, Montoliu I, Chaudry A, Persaud K, Marco S, Chemometr. Intell. Lab. Syst 100 (2010) 28.

[94]. Guo S, Yang D, Zhang S, Dong Q, Li B, Tran N, Li Z, Xiong Y, Zaghloul ME, Adv. Funct. Mater 29 (2019) 1900138.

[95]. Son D, Lee J, Qiao S, Ghaffari R, Kim J, Lee JE, Song C, Kim SJ, Lee DJ, Jun SW, Nat. Nanotechnol 9 (2014) 397. [PubMed: 24681776]

[96]. Matsuhisa N, Chen X, Bao Z, Someya T, Chem. Soc. Rev 48 (2019) 2946. [PubMed: 31073551]

[97]. Kolle M, Lee S, Adv. Mater 30 (2018) 1702669.

[98]. HyungáCheong W, HyebáSong J, JoonáKim J, Nanoscale 8 (2016) 10591. [PubMed: 27166976]

[99]. Jheng L-C, Hsiao C-H, Ko W-C, Hsu SL-C, Huang Y-L, Nanotechnology 30 (2019) 235201. [PubMed: 30721884]

[100]. Lee M-S, Lee K, Kim S-Y, Lee H, Park J, Choi K-H, Kim H-K, Kim D-G, Lee D-Y, Nam S, Nano Lett. 13 (2013) 2814. [PubMed: 23701320]

[101]. Lee M-S, Kim J, Park J, Park J-UNanoscale Res. Letters 10 (2015) 27.

[102]. Chen F, Paronyan TM, Harutyunyan AR, Appl. Phys. Lett 101 (2012), 053119.

[103]. Yi N, Cheng Z, Li H, Yang L, Zhu J, Zheng X, Chen Y, Liu Z, Zhu H,Cheng F, Materials Today Physics, 2020.

[104]. Jang N-S, Kim K-H, Ha S-H, Jung S-H, Lee HM, Kim J-M, ACS Appl. Mater. Interfaces 9 (2017) 19612. [PubMed: 28534393]

[105]. Huang Y, Dong W, Huang T, Wang Y, Xiao L, Su Y, Yin Z, Sensors Actuators A: Phys. 224 (2015) 36.

[106]. Hubbard RS, J. Biol. Chem 43 (1920) 57.

[107]. Gouma P, Kalyanasundaram K, Yun X, Stanacevic M, Wang L, IEEE Sensor. J 10 (2009) 49.

[108]. Weng Y-C, Yang Y-H, Lu I-T, J. Nanosci. Nanotechnol 16 (2016) 7077.

[109]. Cheng Y-K, Lin C-H, Kaneta T, Imasaka T, J. Chromatogr. A 1217 (2010) 5274. [PubMed: 20605024]

[110]. Moon HG, Jung Y, Han SD, Shim Y-S, Shin B, Lee T, Kim J-S, Lee S, Jun SC, Park H-H, ACS Appl. Mater. Interfaces 8 (2016) 20969. [PubMed: 27456161]

[111]. Heaney LM, Ruszkiewicz DM, Arthur KL, Hadjithekli A, Aldcroft C, Lindley MR, Thomas CP, Turner MA, Reynolds JC, Bioanalysis 8 (2016) 1325. [PubMed: 27277875]

[112]. Kahn N, Lavie O, Paz M, Segev Y, Haick H, Nano Lett. 15 (2015) 7023. [PubMed: 26352191]

[113]. Grabowska-Polanowska B, Faber J, Skowron M, Miarka P, Pietrzycka A, Śliwka H, Amann A, J. Chromatogr. A 1301 (2013) 179. [PubMed: 23764192]

[114]. Schon S, Theodore SJ, Güntner AT, Sensor. Actuator. B Chem 273 (2018) 1780.

[115]. Righettoni M, Amann A, Pratsinis SE, Mater. Today 18 (2015) 163.

[116]. Henderson B, Khodabakhsh A, Metsälä M, Ventrillard I, Schmidt FM, Romanini D, Ritchie GA, te Lintel Hekkert S, Briot R, Risby T, Appl. Phys. B 124 (2018) 161. [PubMed: 30956412]

[117]. Lamote K, Brinkman P, Vandermeersch L, Vynck M, Sterk PJ, Van Langenhove H, Thas O, Van Cleemput J, Nackaerts K, van Meerbeeck JP, Oncotarget 8 (2017) 91593. [PubMed: 29207669]

[118]. Agapiou A, Amann A, Mochalski P, Statheropoulos M, Thomas CLP, Trac. Trends Anal. Chem 66 (2015) 158.

[119]. Alberts WM, J. Allergy Clin. Immunol 94 (1994) 289 [PubMed: 8077581]

[120]. Chen X, Feng X, Liu X, Zeng X, Xu Y, Sensor. Actuator. B Chem 295 (2019) 7.

[121]. Zhao Y, Hu J, Tan Z, Liu T, Zeng W, Li X, Huang C, Wang S, Huang Z, Ma W, Sci. Total Environ 668 (2019) 254. [PubMed: 30852202]

[122]. Kim D, Chen Z, Zhou L-F, Huang S-X, Chr. Dis.Trans. Med 4 (2018) 75.

[123]. Deng C, Zhang J, Yu X, Zhang W, Zhang X, J. Chromatogr B 810 (2004) 269.

[124]. Diskin AM, Španěl P, Smith D, Physiol. Meas 24 (2003) 107. [PubMed: 12636190]

[125]. Capone S, Forleo A, Francioso L, Rella R, Siciliano P, Spadavecchia J, Presicce B, Taurino A, J. Optoelectron. Adv. Mater 5 (2003) 1335.

[126]. Güntner AT, Righettoni M, Pratsinis SE, Sensor. Actuator. B Chem 223 (2016) 266.

[127]. Fu XA, Li M, Knipp RJ, Nantz MH, Bousamra M, Cancer Med. 3 (2014) 174. [PubMed: 24402867]

[128]. Chen W, Laiho S, Vaittinen O, Halonen L, Ortiz F, Forsblom C, Groop P, Lehto M, Metsälä M, J. Breath Res 10 (2016), 036011. [PubMed: 27516572]

[129]. Pijnenburg M, Hofhuis W, Hop W, De Jongste JC, Thorax 60 (2005) 215. [PubMed: 15741438]

[130]. Yates DH, Krishnan A, Chow S, Thomas PS, J. Breath Res 5 (2011), 024001. [PubMed: 21498893]

[131]. Kneepkens CF, Lepage G, Roy CC, Free Radic. Biol. Med 17 (1994) 127. [PubMed: 7959173]

[132]. Vreman HJ, Stevenson DK, Oh W, Fanaroff AA, Wright LL, Lemons JA, Wright D, Shankaran S, Tyson JE, Korones SB, Clin. Chem 40 (1994) 1927. [PubMed: 7923774]

[133]. Ghoshal UC, Ghoshal U, Das K, Misra A, (2006).

[134]. Choi K-I, Kim H-J, Kang YC,Lee J-H, Sensor. Actuator. B Chem 194 (2014) 371.

[135]. de Lacy Costello B, Ledochowski M, Ratcliffe NM, J. Breath Res 7 (2013), 024001. [PubMed: 23470880]

[136]. Corradi M, Montuschi P, Donnelly LE, Pesci A, Kharitonov SA, Barnes PJ, Am. J. Respir. Crit. Care Med 163 (2001) 854. [PubMed: 11282756]

[137]. Kim N-H, Choi S-J, Yang D-J, Bae J, Park J, Kim I-D, Sensor. Actuator. B Chem 193 (2014) 574.

[138]. Popa C, Patachia M, Banita S, Matei C, Bratu A, Dumitras D, Laser Phys. 23 (2013) 125701.

[139]. Kim SJ, Koh H-J, Ren CE, Kwon O, Maleski K, Cho S-Y, Anasori B, Kim C-K, Choi Y-K, Kim J, ACS Nano 12 (2018) 986. [PubMed: 29368519]

[140]. Abbas AN, Liu B, Chen L, Ma Y, Cong S, Aroonyadet N, Köpf M, Nilges T, Zhou A, ACS Nano 9 (2015) 5618. [PubMed: 25945545]

[141]. Guo R, Han Y, Su C, Chen X, Zeng M, Hu N, Su Y, Zhou Z, Wei H, Yang Z, Sensor. Actuator. B Chem 300 (2019) 127013.

[142]. Martín-García B, Spirito D, Bellani S, Prato M, Romano V, Polovitsyn A, Brescia R, Oropesa-Nuñez R, Najafi L, Ansaldo A, Small 15 (2019) 1904670.

[143]. Pataniya PM, Tannarana M, Zankat CK, Bhakhar SA, Narayan S, Solanki GK, Patel KD, Jha PK, Pathak VM, J. Phys. Chem. C 124 (2020) 2251.

[144]. Park K-R, Cho H-B,Lee J, Song Y, Kim W-B, Choa Y-H, Sensor. Actuator. B Chem 302 (2020) 127179.

[145]. Basyooni MA, Zaki SE, Ertugrul S, Yilmaz M, Eker YR, Ceram. Int 46 (2020) 9839.

[146]. Wu T, Wang Z, Tian M, Miao J, Zhang H, Sun J, Sensor. Actuator. B Chem 259 (2018) 526.

[147]. Kumar R, Goel N, Kumar M, ACS Sens. 2 (2017) 1744. [PubMed: 29090571]

[148]. Thepnurat M, Chairuangsri T, Hongsith N, Ruankham P, Choopun S, ACS Appl. Mater. Interfaces 7 (2015) 24177. [PubMed: 26457557]

[149]. Cui J, Shi L, Xie T, Wang D, Lin Y, Sensor. Actuator. B Chem 227 (2016) 220.

[150]. Güntner AT, Abegg S, Wegner K, Pratsinis SE, Sensor. Actuator. B Chem 257 (2018) 916.

[151]. Güntner AT, Weber IC, Pratsinis SE, ACS Sens. 5 (2020) 1058. [PubMed: 32172555]

[152]. Yao MS, Tang WX, Wang GE, Nath B, Xu G, Adv. Mater 28 (2016) 5229. [PubMed: 27153113]

[153]. Drobek M, Kim J-H, Bechelany M, Vallicari C, Julbe A, Kim SS, ACS Appl. Mater. Interfaces 8 (2016) 8323. [PubMed: 27003470]

[154]. Assen AH, Yassine O, Shekhah O, Eddaoudi M, Salama KN, ACS Sens. 2 (2017) 1294. [PubMed: 28809112]

[155]. Yassine O, Shekhah O, Assen AH, Belmabkhout Y, Salama KN, Eddaoudi M, Angew. Chem 128 (2016) 16111.

[156]. Maier I, Fieber 11 (1988) 566.

[157]. Yamazoe N, Shimanoe K, Sensor. Actuator. B Chem 128 (2008) 566.

[158]. Schierbaum K, Weimar U, Göpel W, Sensor. Actuator. B Chem 2 (1990) 71.

[159]. Yang D, Fuadi MK, Kang K, Kim D, Li Z, Park I, ACS Appl. Mater. Interfaces 7 (2015) 10152. [PubMed: 25902930]

[160]. Zhang D, Liu J, Jiang C, Liu A, Xia B, Sensor. Actuator. B Chem 240 (2017) 55.

[161]. Peng G, Tisch U, Adams O, Hakim M, Shehada N, Broza YY, Billan S, Abdah-Bortnyak R, Kuten A, Haick H, Nat. Nanotechnol 4 (2009) 669. [PubMed: 19809459]

Fig. 1. Stretchable gas sensors enabled by direct integration of gas-sensitive nanomaterials onto the stretchable substrate (template) or by the exploration of stretchable structures.

The stretchable substrate template in the former can be thin films (with a microtectonic sensing layer), textiles, porous (fibrous) structures. Reprinted with permissions from Refs. [68-70]. The commonly used stretchable structures in the latter include wrinkled surfaces, island-bridge layouts, strain isolation layers, or their combinations as in the stretchable laser-induced graphene (LIG) gas sensing platform. Reprinted with permissions from Refs. [71-73].

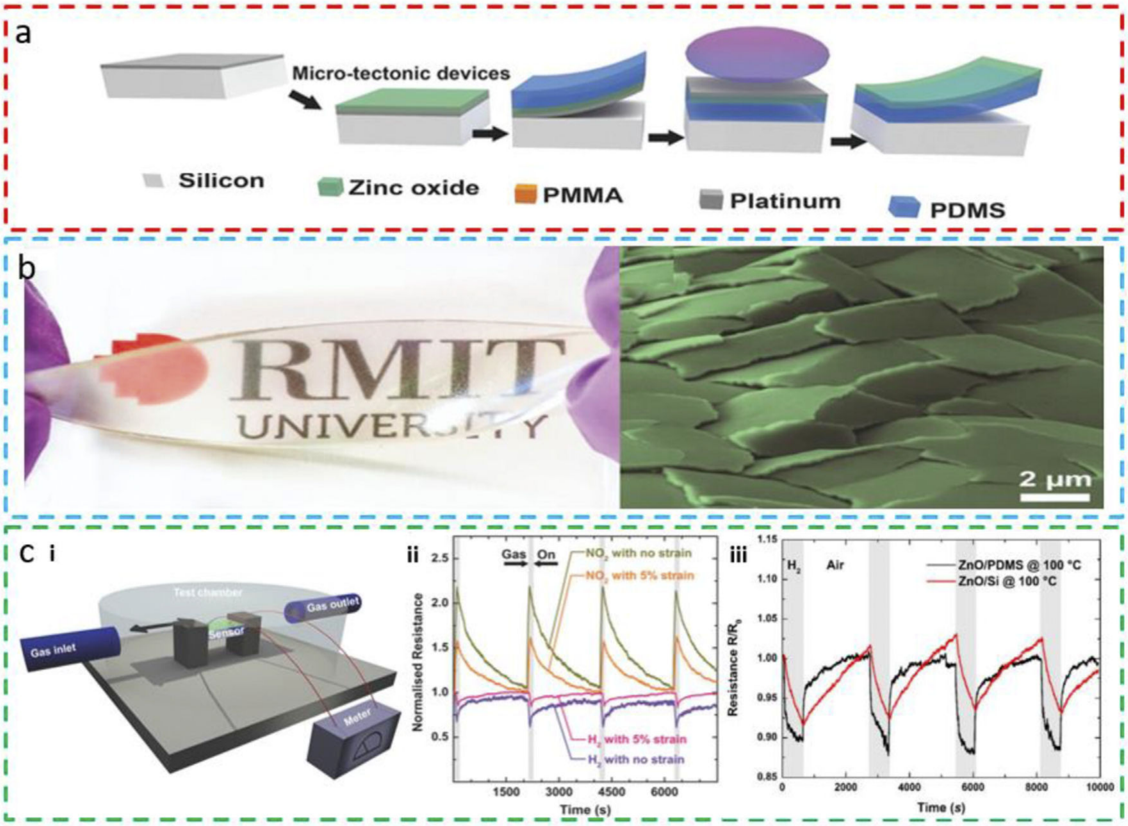

Fig. 2. Stretchable microtectonic ZnO-based gas sensor.

(a) The fabrication process of the stretchable gas sensor. After depositing a 50 nm-thick Pt layer on the Si wafer, ZnO thin film is sputter-deposited at 250°C, followed by peeling off of the ZnO/Pt layer with polydimethylsiloxane (PDMS). Removal of the Pt layer by reactive ion etching and release of the device from the wafer complete the fabrication process. **(b)** Optical image of the transparent and twisted microtectonic ZnO device and false-color scanning electron microscope (SEM) image of the surface-cracked microtectonic surface of ZnO. **(c)** Testing of the gas sensors in **(i)** a controlled gas flow test chamber. **(ii)** Microtectonic sensor response to H_2 and NO_2 in relaxed and stretched states at room temperature (shaded areas for an exposure of 80 s). **(iii)** Comparison of hydrogen sensing performance between a stretchable microtectonic ZnO/PDMS gas sensor and a rigid ZnO/Si sensor at an elevated temperature of 100°C. Reprinted with permission from Ref. [68].

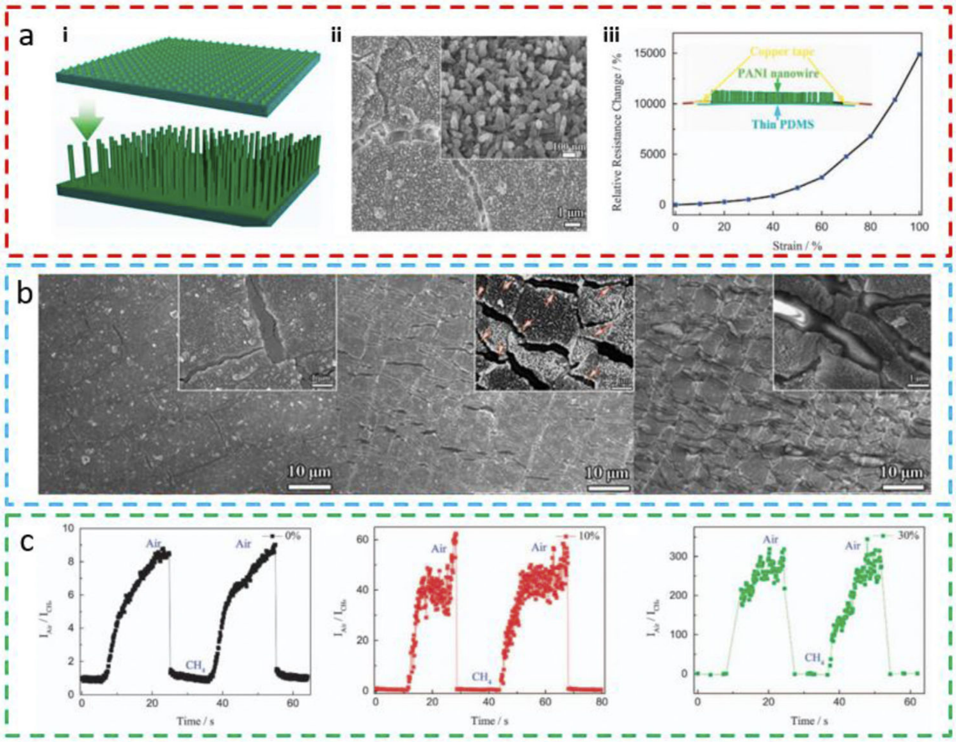

Fig. 3. Stretchable methane (CH_4) sensor based on the polyaniline (PANI) nanowire array.
(a) The formation process of the PANI nanowire array through **(i)** a chemical oxidation polymerization process. **(ii)** SEM images of the PANI nanowire array on a PDMS substrate, with the high-magnification SEM image of the nanowire shown in the inset. **(iii)** The plot of the relative resistance change versus strain for the PANI nanowire array. **(b)** SEM images of the PANI nanowire array film under different strains of 0%, 40%, and 80%. **(c)** Time-dependent response and recovery curves of the PANI nanowire array-based sensor exposed to CH_4 gas under a tensile strain of 0%, 10%, and 30%. Reprinted with permission from Ref. [74].

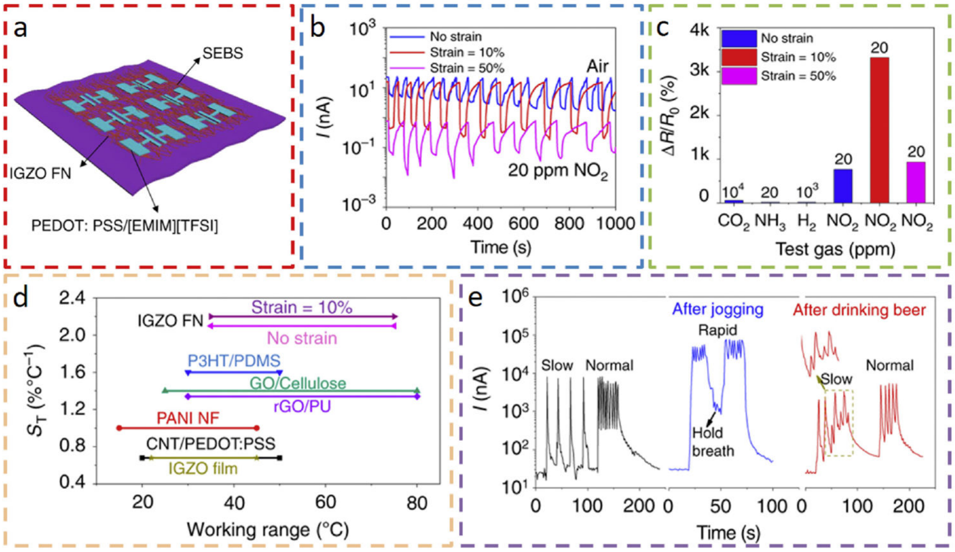

Fig. 4. Schematic and sensing performance of an indium-gallium zinc oxide (IGZO) nanofiber network (FN) sensor on a poly[styrene-b-(ethylene-co-butylene)-b-styrene] (SEBS) substrate.
(a) Schematic of the stretchable IGZO FN sensor and **(b)** its current response to 20 ppm NO_2 for an applied tensile strain of 0%, 10%, and 50%, along with **(c)** its selectivity to 20 ppm NO_2 against 20 ppm NH_3, 1000 ppm H_2, and 10,000 ppm CO_2. **(d)** Comparison of the sensitivity of the temperature sensor with literature reports. **(e)** The current response from the IGZO FN sensor exposed to exhaled gas during respiration. Reprinted with permission from Ref. [75].

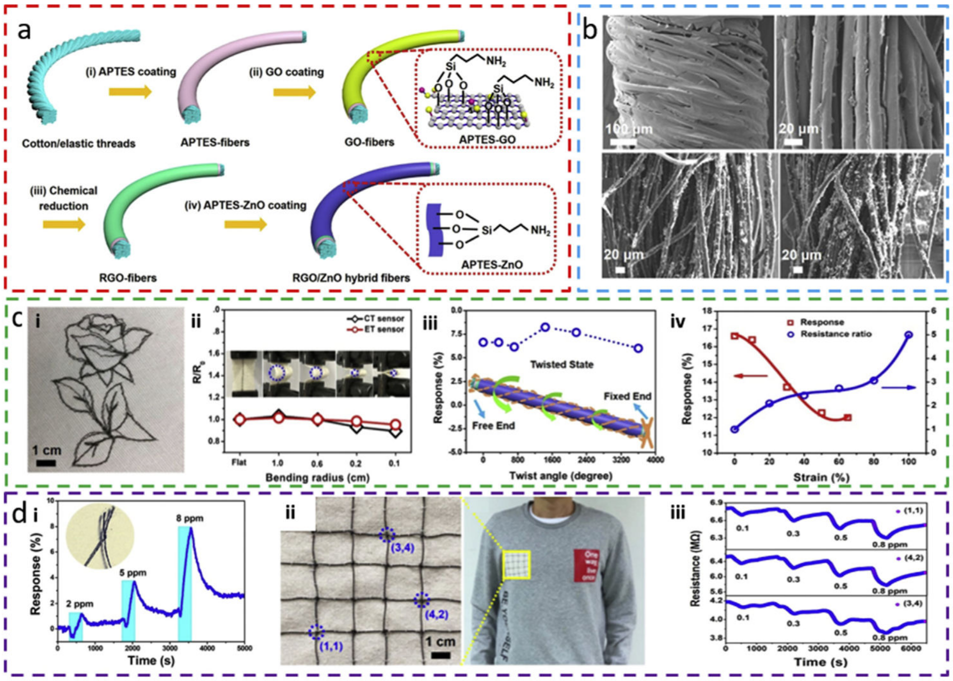

Fig. 5. Stretchable NO_2 sensor weavable onto cloths.

(a) Schematic diagram of the fabrication process for reduced graphene oxide (rGO)/ZnO hybrid fibers. **(b)** SEM images of rGO/ET and rGO/CT sensors and rGO/ZnO CT sensors with a coating time of 3 h and 4 h. ET: elastic thread; CT: cotton thread. **(c)** Deformation test of rGO/ZnO CT sensors and rGO/ZnO ET sensors that **(i)** can be woven onto fabric to form a designed pattern. **(ii)** The relative resistance change of rGO/ZnO CT and ET sensors versus the bending radius, with pictures of the sensor bent at different radii shown in the inset. **(iii)** Sensor response for a twist angle up to 3600° in 2 ppm NO_2. (iv) rGO/ZnO ET gas sensor response and relative resistance change as a function of tensile strain when exposed to 4 ppm NO_2. **(d)** Scalable application of CT/ET sensors for NO_2 detection. **(i)** Gas sensor response from an integrated sensor by knotting the fractured CT sensor together. The inset shows the image of the knotted CT sensor. **(ii)** Optical image of a 4 × 4 ET sensor array network that is stitched onto the dressings. **(iii)** Gas sensing properties of selected units in the 4 × 4 gas sensor array. Reprinted with permission from Ref. [69].

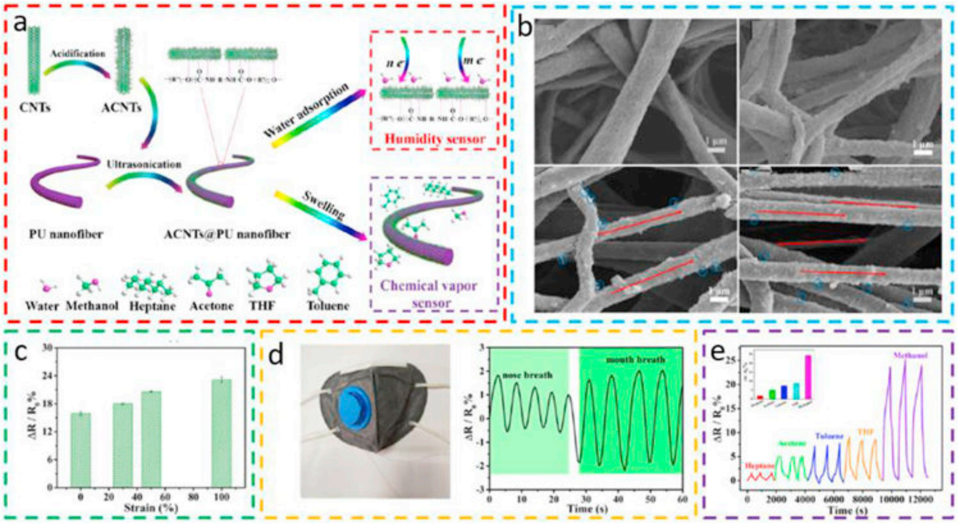

Fig. 6. Stretchable volatile organic compounds (VOCs) detector based on an electrospun fiber network structure.

(a) Schematic demonstration of the preparation process of the conductive nanofiber composite (CNC) (left) and its sensing mechanisms for humidity and chemical vapors (right). **(b)** SEM images of CNC fibers under a tensile strain of 0%, 30%, 50%, and 100%. **(c)** The response of the CNC fiber sensor to a relative humidity of 59% at different strains. **(d)** Photograph of a breathing mask with CNC-based humidity sensor incorporated inside the mask and its sensing response to nose breath and mouth breathing. **(e)** Chemical vapor sensing of the CNC-based sensor to different types of VOCs at a fixed concentration of 30 ppm. Reprinted with permission from Ref. [60].

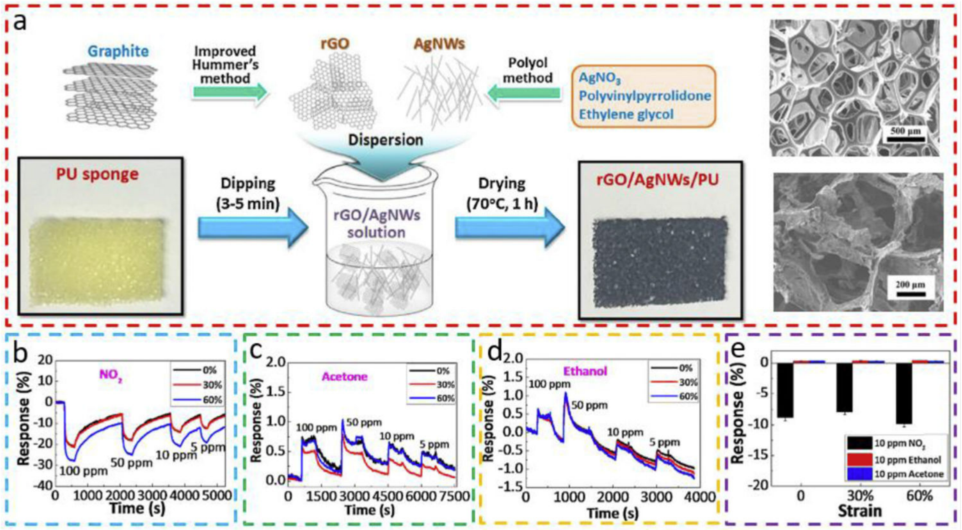

Fig. 7. Stretchable gas sensor fabricated on a porous sponge template.

(a) Schematic to show the fabrication process of rGO/silver nanowires (AgNWs)-PU composites. SEM images of the PU sponge before and after the coating of rGO/AgNW. Stretching-dependent responses of rGO/AgNW-PU composite to **(b)** NO_2, **(c)** acetone, and **(d)** ethanol at different concentrations. **(e)** Comparison of responses of rGO/AgNW-PU composite to NO_2 of 10 ppm, ethanol of 10 ppm, and acetone of 10 ppm at a tensile strain of 0%, 30%, and 60%. Reprinted with permission from Ref. [70].

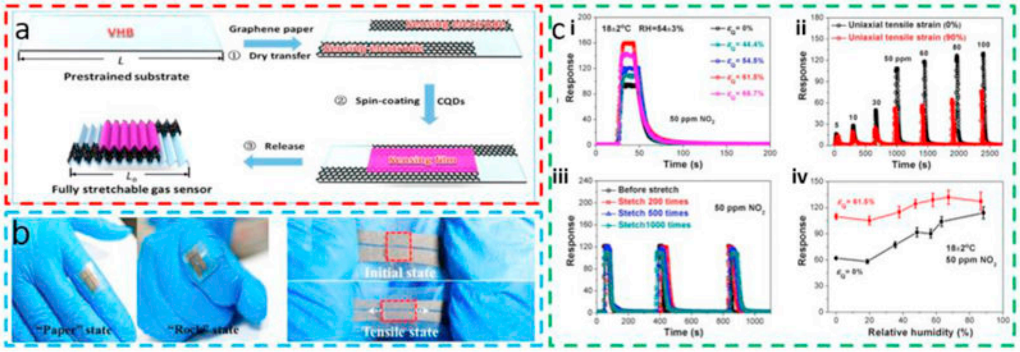

Fig. 8. Fully stretchable and humidity-resistant quantum dot wrinkled gas sensors from a uniaxial pre-strain strategy.

(a) Schematic to show the fabrication process of the fully stretchable gas sensor and **(b)** its stretchable demonstration, with photographs of the gas sensor attached on the finger joint with "paper" and "rock" states and under repeated tensile cycling. **(c)** Responses of the stretchable gas sensor **(i)** created by different level of pre-strains (i.e., 0%, 44.4%, 54.5%, 61.5%, and 66.7%), **(ii)** to different concentrations of NO_2 at a uniaxial tensile strain of 0% (black) or 90% (red), **(iii)** after different times of repeated stretching of 20% (pre-strain of 54.5%); **(iv)** at different relative humidity created by a pre-strain of 0% (black) or 61.5% (red). Note: NO_2 of 50 ppm is used in the above testing unless otherwise specified. Reprinted with permission from Ref. [71].

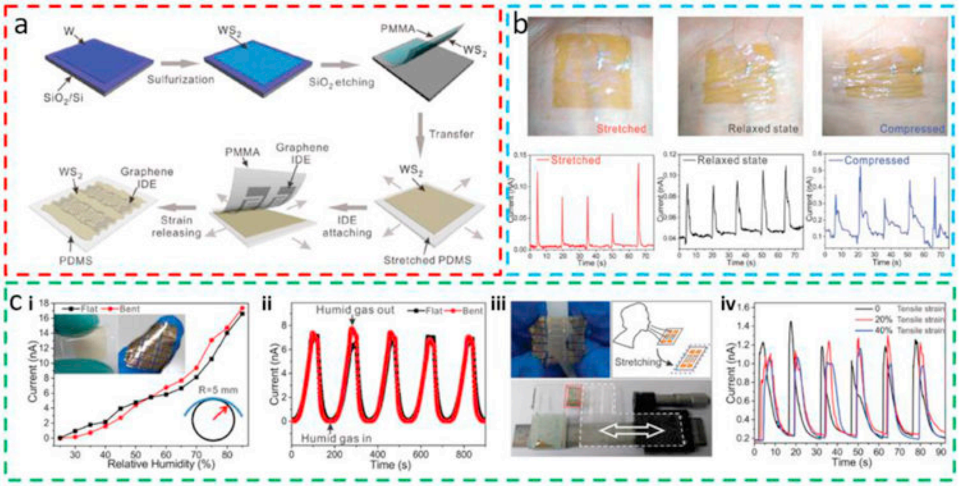

Fig. 9. Stretchable humidity sensor based on wrinkled WS_2 from the biaxial pre-strain strategy. **(a)** The fabrication process of the 2D WS_2-based stretchable gas sensor. After the deposition of an ultrathin W film on the SiO_2/Si substrate, sulfurization ofW results in WS_2 thin film, followed by peeling off with PMMA. After the transfer of the WS_2 thin film and then the patterned graphene onto a biaxially pre-stretched PDMS substrate, the release of the pre-strain yields a transparent, stretchable WS_2 humidity sensor. **(b)** Image of the WS_2 humidity sensor in stretched, relaxed, and compressed states with the corresponding humidity response, respectively. **(c)** The (**i, ii**) flexible and (**iii, iv**) stretchable demonstrations of the biaxially wrinkled WS_2 sensor. **(i)** The current response of the sensor in flat and bent states (images of the sensor shown in the insets) and **(ii)** the dynamic response from the sensor over multiple cycles. **(iii)** The stretched WS_2 humidity sensor and **(iv)** its humidity response for a tensile strain of 0, 20%, and 40%. Reprinted with permission from Ref. [86].

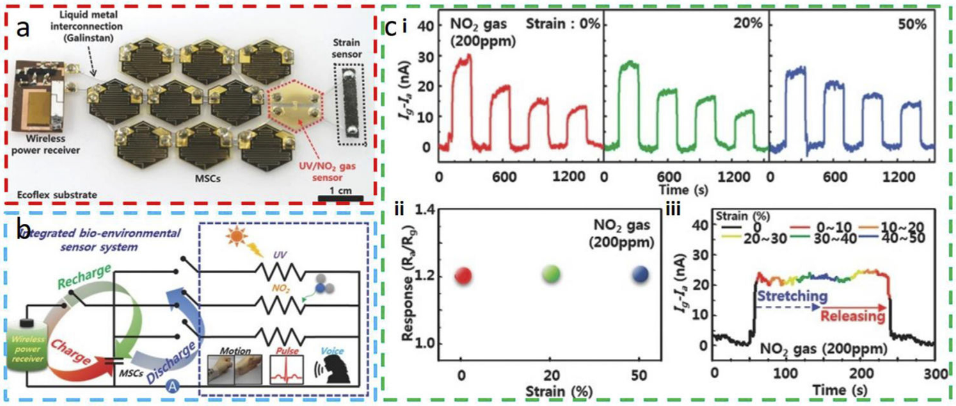

Fig. 10. Multifunctional stretchable sensor system integrated with a radio frequency (RF) rechargeable micro-supercapacitor (MSC) array.

(a) Photograph and **(b)** circuit diagram of the sensor system consisting of an MSC array, an RF power receiver, a strain sensor, an ultraviolet (UV)/NO_2 gas sensor. **(c)** Characterization of the NO_2 gas sensor based on multi-walled carbon nanotube (MWNT)/SnO_2 NW hybrid film to NO_2 of 200 ppm, with **(i)** its current and **(ii)** resistant responses for a tensile strain of 0%, 20%, and 50%, along with **(iii)** the current response under a dynamic stretching up to 50% followed by a release. Reprinted with permission from Ref. [72].

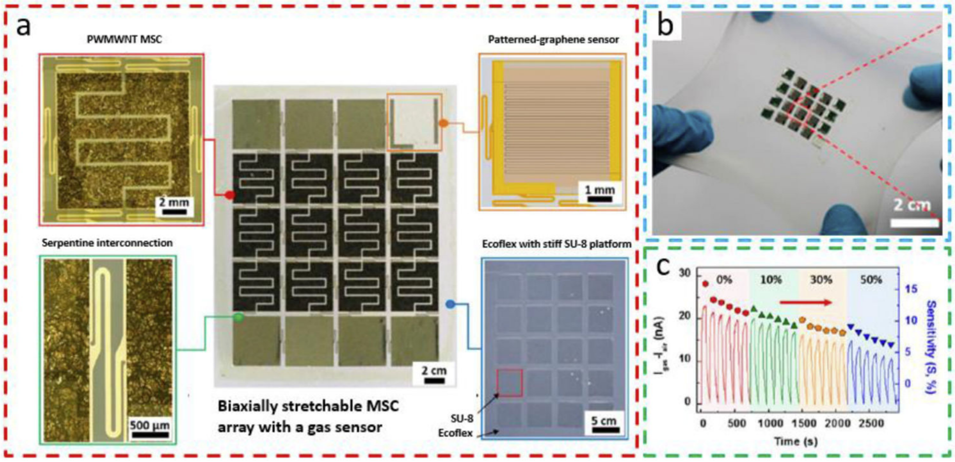

Fig. 11. Biaxially stretchable graphene NO_2 sensor powered by MSC on a soft Ecoflex substrate with an embedded SU-8 island array.

(a) The layout of (center) biaxially stretchable device consisting of polyaniline-wrapped MWNT (PWMWNT) MSC array, graphene gas sensor. serpentine interconnects between device islands, all on the Ecoflex substrate with an embedded stiff SU-8 array. **(b)** Optical image of the device system under a biaxial tensile strain of 40%. **(c)** Dependence of I_{gas}-I_{air} (left y-axis) and sensitivity (right y-axis) of the gas sensor for consecutive exposure to NO_2 as the tensile strain increases from 0 to 50%. Reprinted with permission from Ref. [87].

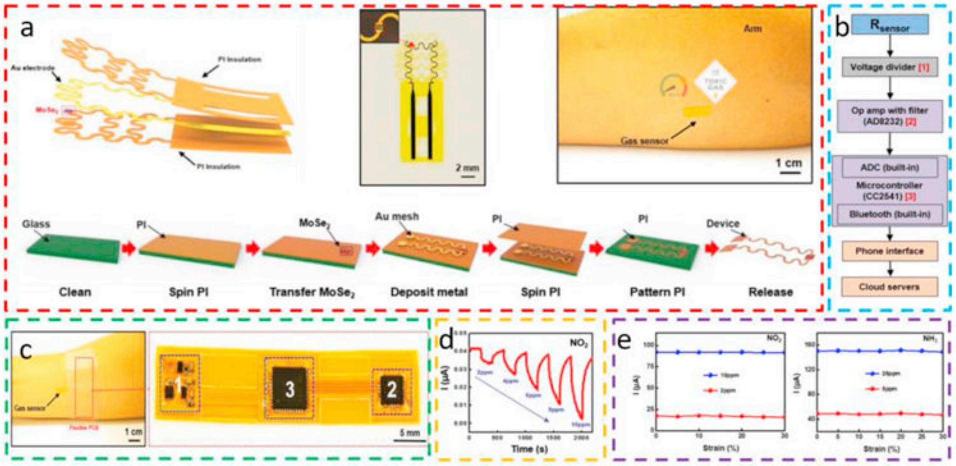

Fig. 12. Stretchable $MoSe_2$-based NO_2 sensor with a serpentine Au mesh connected to built-in signal processing circuits.

(a) 3D schematic, optical image, and fabrication process of the $MoSe_2$-based gas sensor with serpentine Au mesh encapsulated between polyimide (PI) layers to be positioned at the neutral mechanical plane. **(b)** Block diagram of the circuit design for data processing and delivery. **(c)** Optical images of the assembled device with the gas sensor connected to a flexible PCB under the bandage (1: voltage divider; 2: amplifier; 3: microcontroller). Current responses of the gas sensor to **(d)** NO_2 of different concentrations and **(e)** tensile strain from 0 to 30% (left: NO_2; right: NH_3). Reprinted with permission from Ref. [94].

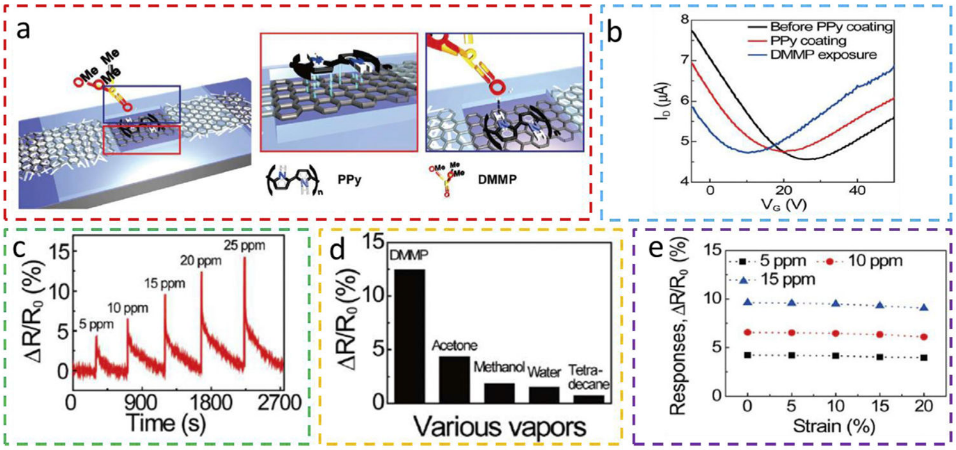

Fig. 13. Stretchable dimethyl methylphosphonate (DMMP) gas sensor with strain isolation around the gas sensing region based on graphene/AgNW decorated with polypyrrole (PPy).
(a) Schematic of the graphene channel decorated with PPy (left) with π-π stacking interaction (red box), which can bond to DMMP through a hydrogen bonding (blue box). **(b)** The surface coating conditions of the graphene channel can affect the transfer characteristics of the field-effect transistor (FET) sensors. Responses of the stretchable graphene/PPy gas sensors to **(c)** DMMP of different concentrations, **(d)** DMMP as compared to other gaseous vapors (e.g., acetone, methanol, water, and tetradecane, all of 20 ppm), and **(e)** a tensile strain up to 20% for a DMMP concentration of 5, 10, and 15 ppm. Reprinted with permission from Ref. [98].

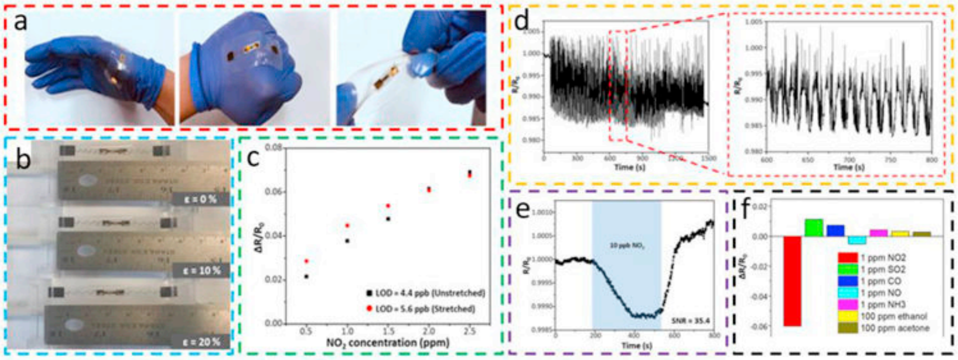

Fig. 14. Stretchable rGO/MoS_2-based gas sensor with serpentine interconnects on a soft substrate with a rigid glass surface inclusion.

(a) Optical images of the gas sensor conformed to the hand upon bending to the fist and twisting. **(b)** Pictures showing the gas sensor stretched to a tensile strain of 0%, 10%, and 20%, and **(c)** its responses to NO_2 from 0.5 to 2.5 ppm before and after a tensile strain of 20% to indicate an improvement in the calculated limit of detections. **(d)** Resistance variation during a 20% cyclic strain test. **(e)** The measurement of the gas sensor to NO_2 of 10 ppb with an excellent signal-to-noise ratio of 35.4. **(f)** The selectivity of the stretchable rGO/MoS_2 gas sensor. Reprinted with permission from Ref. [103].

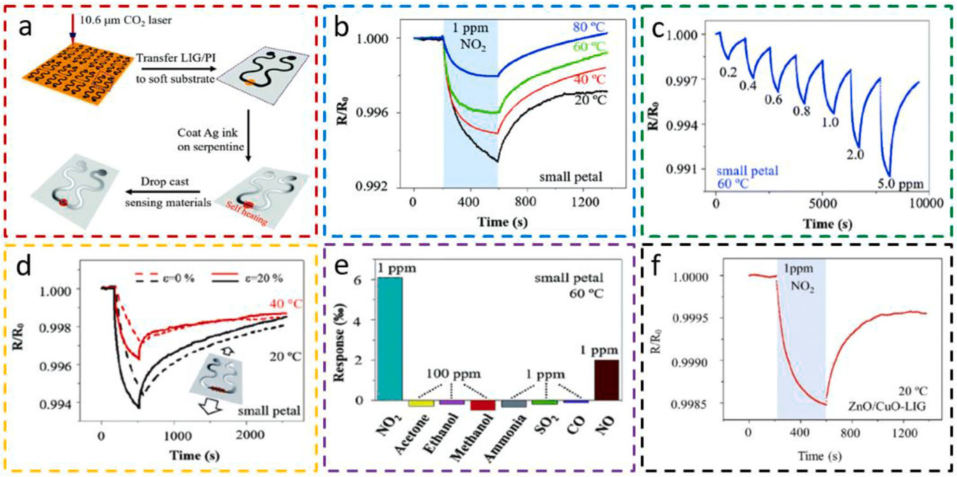

Fig. 15. Stretchable laser-induced graphene (LIG) gas sensing platform.

(a) Schematic to show the fabrication process of the LIG gas sensing platform. After creating a porous LIG pattern on a PI film by laser scribing, the LIG/PI composite is transferred to a soft substrate, followed by coating the serpentine regions with conductive metal and drop-casting of gas-sensitive nanomaterials in the sensing region. Responses of the stretchable LIG gas sensing platform with small petal rGO/MoS_2 nanoflowers **(b)** at various temperatures from self-heating, **(c)** to NO_2 from 0.2 to 5 ppm at 60°C, and **(d)** before and after a uniaxial tensile strain of 20% at room temperature (black) and 40°C (red). The selectivity of the **(e)** rGO/MoS_2 and **(f)** ZnO/CuO on the LIG gas sensing platform to a wide range of gaseous molecules. Note: 1 ppm NO_2 is used in the testing unless otherwise specified. Reprinted with permission from Ref. [73].

Table 1

Common gaseous biomarkers from the human body for disease diagnostics.

Disease	Biomarker	Concentration (healthy)	Concentration (diseased)	Ref
Diabetes	Acetone	300–900 ppb	>1800 ppb	[123,124]
Liver failure	NH_3	10 ppb	1000 ppb	[125,126]
Lung cancer	2-butanone	0.45–2.34 nmol/L	1.78–8.38 nmol/L	[127]
End-stage renal disease	NH_3	74–2935 ppb	820–14700 ppb	[128]
Asthma	NO	15 ppb	>30 ppb	[129]
Bronchiolitis obliterans syndrome	NO	11.4 ± 4.9 ppb	24.3 ± 13.2 ppb	[130]
Lipid peroxidation	Hydrocarbons	~ppb	~ppb	[131]
Ovarian cancer	Styrene,	~ppb	~ppb	[112]
Chronic kidney disease	Trimethylamine	none	1.76–38.02 ppb	[113]
Hemolytic disease	CO	1.0 ± 0.7 μL	1.8 ± 0.8 μL/L	[132]
Small intestinal bacterial overgrowth	H_2	–	>12 ppm	[133]
Halitosis	H_2S	–	0.1–0.5 ppm	[134]
Methanogens	Methane	–	16.6 ppm	[135]
Cystic fibrosis	NO/NO_2	–	0.35 ± 0.07 μM	[136]
Lung cancer	Toluene	20–30 ppb	80–100 ppb	[137]
Renal failure	Ethylene	6.3 ppb	>0.1 ppm	[138]